Geological and geochemical characteristics and formation mechanisms of the Zhaishang Carlin-like type gold deposit, western Qinling Mountains, China

Jiajun Liu [a,b,c,*], Hongzhang Dai [a,c], Degao Zhai [a,c], Jianping Wang [a,c], Yinhong Wang [a,c], Longbo Yang [d], Guangjian Mao [a,c], Xinhui Liu [e], Yanfu Liao [d], Chao Yu [a,c], Qiangzhi Li [f]

[a] State Key Laboratory of Geological Processes and Mineral Resources, China University of Geosciences, Beijing 100083, People's Republic of China
[b] State Key Laboratory of Ore Deposit Geochemistry, Institute of Geochemistry, Chinese Academy of Sciences, Guiyang 550002, People's Republic of China
[c] School of Earth Sciences, China University of Geosciences (Beijing), Beijing 100083, People's Republic of China
[d] Department of Earth & Planetary Sciences, McGill University, Montreal H3A2A7, Canada
[e] No. 5 Gold Geological Party of Chinese Armed Police Force, Xi'an 710100, People's Republic of China
[f] Gold Headquarters of Chinese Armed Police Force, Beijing 100102, People's Republic of China

ARTICLE INFO

ABSTRACT

Located in the western part of the Min–Li metallogenic belt within the western Qinling Mountains, the Zhaishang gold deposit is a giant Carlin-like disseminated gold deposit discovered recently. The ore deposit is present both in rocks of low grade metamorphic Middle Devonian and Lower Permian clastic formation, which is composed of quartz sandstone, siltstone, calcareous slate and argillaceous limestone. Gold mineralization is strictly controlled by a fault zone. Minerals in ores are quite complex and consist of sulfides, sulfosalt, oxides, sulfate, carbonate, tungstate, telluride, native metals, and polymetallic alloys. The diversity of mineral in the ores and the existence of microscopic visible native gold constitute the outstanding features of the gold deposit.

We believe that the mineral source of the ore deposit has a close connection with the host rocks, because all samples show the light of the REE distribution patterns. The S, C, Pb, H and O isotopic compositions show that the ore-forming elements were mainly derived from the country rocks, the underlying rocks, and partially deep sources. Data obtained suggest that the ore-forming fluids were derived predominantly from an active meteoric groundwater system. Mineralization and related alteration have features of a low water/rock ratio. Ore-forming temperatures are estimated to have been in the range from 120 to 240 °C. The dissolution of ferruginous limestone in the host rocks and the sulfidation of the dissolved iron by H_2S introduced by ore fluids constituted not only the most important depositional mechanisms for the existence of microscopic visible gold grains but also favorable conditions for gold enrichment in the Zhaishang gold deposit.

© 2014 Elsevier B.V. All rights reserved.

1. Introduction

Many large Carlin-like or sedimentary rock-hosted (Peters et al., 2002a,b) gold deposits (Chen et al., 2004; Khin et al., 2007a,b) are present in the western part of the Qinling Orogen. In the past 30 years, many additional gold deposits and prospects have been discovered in the Qinling fold belt (Fig. 1, Table 1). The gold resource of Yangshan is more than 300 t (Li et al., 2014; Liang et al., 2014). Similar gold deposits, such as Jinlongshan (109 t; Liu, 2006), and Baguamiao (106 t; Zhang et al., 2003), Dashui (90.5 t, Liang, 2011), Zaozigou (86 t, Liang, 2011), Shuangwang (70 t; Liu et al., 2011a), Dongbeizhai (70 t; Zheng et al., 1994; Khin et al., 2007b), Daqiao (67 t, Liang, 2011), Ma'anqiao (>50 t,

Zhu et al., 2009), La'erma (>50 t; Liu et al., 2000a; Yin, 2004), Manaoke (40 t; Xiao et al., 2008), Huachanggou (35 t, Liu et al., 2013; Xiao et al., 2008), Liba (>28 t; Chen et al., 2004), Lu'erba (23 t; Yin, 2004), Qiaoqiaoshang (>20 t; Khin et al., 2007b; Zheng et al., 1994), and Jiawu (>20 t; Yan et al., 2011) are also identified, and therefore demonstrate a significant exploration potential for such deposits throughout the western Qinling fold belt (Liu et al., 2008a). The Zhaishang gold deposit, in Gansu Province, was discovered by the No. 5 Gold Geological Party of the Chinese Armed Police Force and recognized as a giant Carlin-like type gold deposit in the Qinling fold belt with 127 t Au proven reserves, and a geologically-inferred resource of at least 198 t of Au (Liu et al., 2011b; Yue et al., 2013). The deposit was discovered in 2003, by a follow-up of gold geochemical stream anomalies (Yang and Zheng, 2003). The discovery marked an important breakthrough in prospecting for Carlin-like gold deposits over the past decade in the western Qingling Mountains, China (Lu et al., 2006). This research on

* Corresponding author at: State Key Laboratory of Geological Processes and Mineral Resources, China University of Geosciences, Beijing 100083, People's Republic of China.
E-mail address: liujiajun@cugb.edu.cn (J. Liu).
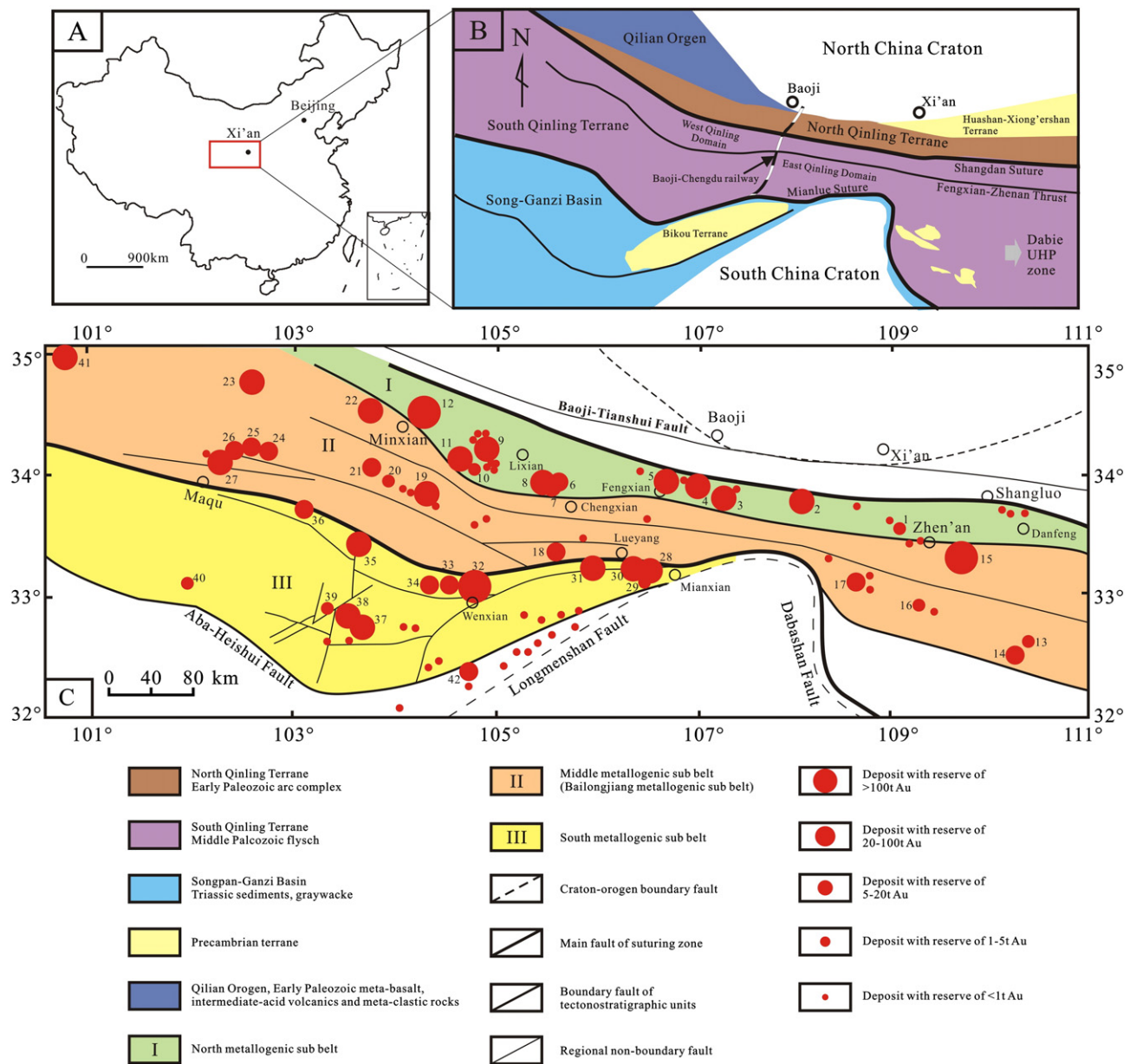
Fig. 1. Schematic map showing the tectonics and distribution of Carlin and Carlin-like gold deposits in West Qinling Mountains. Modified after Chen et al. (2004).

its metallogenic characteristics and genetics will further enhance prospecting for gold in the region.

2. Regional geology

The Qinling Orogen is bound to the northwest by the NW-trending Qilian Orogen (Zhang et al., 1995), to the southwest by the Aba–Heishui Fault of the Songpan–Ganzi Basin (Yang et al., 1996), and to the east it extends into the Dabie Ultra-High Pressure (UHP) zone (Fig. 1B, Zhang et al., 1995). The Qinling Orogen and Dabie-UHP zone collectively constitute the collision zone between the North and South China cratons in central China (Gao et al., 1996; Heberer et al., 2014; Xu et al., 2002a,b; Zhang et al., 2004). The South and North China cratons first collided in the Permian near their eastern ends, which then progressively scissored together as the South China craton rotated clockwise with respect to the North China craton (Peters et al., 2013; Zhao et al., 2013). This collisional event was protracted, starting in the east within the Dabie–Sulu UHP zone and culminating in the west within the

Qinling Orogen in a progressive process event called "scissor suturing" (Chen et al., 2006; Zhang et al., 2004; Zhu et al., 1998). However, the Qinling Orogen has low-grade metamorphism and widespread Triassic intrusions in contrast with the Dabie-UHP zone, which is characterized by coesite, diamond, and other UHP minerals (Su et al., 2010; Zheng, 2008), and limited Triassic magmatism.

Field studies of the Qinling Orogen have identified suture zones that divide the orogen into the North Qinling Terrane and South Qinling Terrane via the Shangdan Suture (Gao et al., 1996; Liu and Zhang, 2013). The North Qinling Terrane consists of an early Paleozoic arc that was accreted to the North China Craton at ca. 450 Ma along the Shangdan Suture (Zhang et al., 2000). This area hosts minor gold mineralization (Mao et al., 2002). The South Qinling Terrane is further subdivided into the central domain and southern domain along the Zhenan–Fengxian Fault. The central domain, which is included by Mei et al. (1999) in the northern zone of the South Qinling Terrane, is dominated by flysch and other clastic rocks that accumulated in a late Paleozoic basin between the converging cratonic blocks. The southern domain is

Table 1
Distribution of Carlin and Carlin-like type gold deposits in western Qinling Mountains.

No.	Deposit	Location	Resource (t)	Scale	Type	References
1	Er'taizi	Zhen'an	1.5	Small	Carlin-like	Li et al. (2001)
2	Ma'anqiao	Zhouzhi	>50	Large	Carlin-like/orogenic	Zhu et al. (2009)
3	Shuangwang	Taibai	>70	Large	Carlin-like	Liu et al. (2011a)
4	Baguamiao	Fengxian	106	Giant	Carlin-like	Zhang et al. (2003)
5	Pangjiahe	Fengxian	37	Large	Carlin-like	Xiao et al. (2008)
6	Xiaogouli	Xicheng	15	Middle	Carlin	Xiao et al. (2008)
7	Anjiacha	Xihe	8.7	Middle	Carlin	Wang et al. (1998)
8	Daqiao	Xihe	67	Large	Carlin-like	Liang (2011)
9	Liba	Lixian	>28	Large	Carlin-like	Chen et al. (2004)
10	Maquan	Lixian	7.5	Middle	Carlin-like	Ma et al. (1997)
11	Jinshan	Lixian	31	Large	Carlin-like	Xiao et al. (2008)
12	Zhaishang	Minxian	127	Giant	Carlin-like	Liu et al. (2011a,b), Yue et al. (2013)
13	Yindonggou	Yunxian	15	Middle	Carlin-like	Qin and Lei (1996)
14	Xujiapo	Yunxian	2.5	Small	Carlin-like	Cai et al. (1999)
15	Jinlongshan	Zhen'an	109	Giant	Carlin	Liu (2006)
16	Linxiang	Xunyang		Small	Carlin	Zou et al. (2000)
17	Huanglong	Hanyin	5	Middle	Carlin	Zhang et al. (2001)
18	Shangjiagou	Kangxian		Middle	Carlin	Shao and Wang (2001)
19	Pingding	Zhouqu	20.8	Large	Carlin	Xiao et al. (2008)
20	Lazikou	Diebu		Small	Carlin	Wang et al. (1998)
21	Zaibu	Diebu	5	Middle	Carlin	Chen et al. (2004)
22	Luer'ba	Minxian	23	Large	Carlin	Yin (2004)
23	Zaozigou	Hezuo	86	Large	Carlin	Liang (2011)
24	Qiongmo	Ruo'ergai	12	Middle	Carlin	Liu et al. (2000a), Xiao et al. (2008)
25	La'erma	Luqu	>50	Large	Carlin-like	Liu et al. (2000a), Yin (2004)
26	Zhongqu	Luqu	>50	Large	Carlin-like	Yin (2004)
27	Dashui	Maqu	90.5	Large	Carlin-like	Liang (2011)
28	Jianchalin	Lveyang	98	Large	Carlin-like	Xiao et al. (2008)
29	Lijiagou	Mianxian	1	Small	Carlin	Wang et al. (1998)
30	Donggouba	Lveyang	25	Large	Carlin-like	Xiao et al. (2008)
31	Huachanggou	Lveyang	35	Large	Carlin-like	Xiao et al. (2008), Liu et al. (2013)
32	Yangshan	Wenxian	>300	Giant	Carlin	Li et al. (2014)
33	Shijiba	Wenxian	10.9	Middle	Carlin	Xiao et al. (2008)
34	Lianhecun	Nanping	10	Middle	Carlin	Chen et al. (2004)
35	Manaoke	Nanping	40	Large	Carlin	Xiao et al. (2008)
36	Baxi	Ruo'ergai	15.3	Middle	Skarn/Carlin	Xiao et al. (2008)
37	Qiaoqiaoshang	Songpan	>20	Large	Carlin	Zheng et al. (1994), Khin et al. (2007b)
38	Dongbeizhai	Songpan	70	Large	Carlin	Zheng et al. (1994), Khin et al. (2007b)
39	Zeboshan	Songpan	2	Small	Carlin	Ji et al. (1998)
40	Jinmuda	A'ba		Small	Carlin	Zhang et al. (2002a)
41	Jiawu	Tongde	>20	Large	Carlin-like	Yan et al. (2011)
42	Jindonggou	Pingwu	>5	Middle	Carlin-like	Huang et al. (2010)

covered by Paleozoic rocks in the east and characterized by the eastern-most exposure of Triassic turbiditic deposits in the west that are partly calcareous and form part of the immense Songpan–Ganzi Basin (Fig. 1B, Zeng et al., 2012). Geographically, the South Qinling Terrane is subdivided into the West and East Qinling domains approximately at the Baoji–Chengdu Railway (Fig. 1B; Zhang et al., 1995; Zheng et al., 2010). The southern boundary of the Qinling Orogen is also a suture known as the Mianlue Suture that separates the orogen from the South China Craton (Dong et al., 2011; Liu and Zhang, 2013).

The Shangdan Suture is interpreted to have formed following subduction of the Shangdan Ocean during Early Silurian time (457–422 Ma; Dong et al., 2011; Mao et al., 2008; Qiu and Wijbrans, 2006). The Shangdan Suture is defined by a linear, patchy distribution of arc-related volcanic rocks and ophiolites, which crop out at Yuanyangzhen, Wushan, Guanzizhen, Tangzang, Yanwan, Heihe and Danfeng (Dong et al., 2011).

The Mianlue Suture is a younger structure that developed between the South and North China cratons following the northward subduction of the Palaeo-Mianlue Ocean during Late Triassic time between 254 and 220 Ma (Ames et al., 1993; Li et al., 1996). Ophiolites in the Mianlue Suture include strongly sheared metabasalt, gabbro, ultramafic rocks and radiolarian cherts (Dong et al., 2011; Meng and Zhang, 2000; Qin et al., 2009). The Late Triassic collisional orogenesis is associated with

a widespread granitic magmatism and extensive fold-and-thrust deformation throughout the Qinling Orogen (Qin et al., 2009).

The West Qinling Orogen (WQO) is bounded by the Linxia–Wushan–Tianshui Fault to the north and the Mianlue Suture to the south (Li et al., 2007; T. Yang et al., 2013). The domain consists of Devonian–Cretaceous sedimentary units. Faults are well developed in the domain and their overall trend is consistent with regional tectonic trends marking the boundaries of major regional lithologies. The faults are structural sites that control the location of regional magmatism where Late Triassic granites are widespread. The granites comprise a 400-km-long granitic belt between the Shangdan and Mianlue sutures, and >200 plutons crop out in an area totaling 4000 km^2 (Zhang et al., 2009).

Voluminous magmatic rocks, dominated by granitic plutons and felsic porphyries with minor volcanic rocks and dykes, were emplaced during the Mesozoic in the eastern Qinling Mountains. They can be divided into two main stages according to their isotopic ages: 240–190 Ma and 160–110 Ma (Han et al., 2007, 2013; Heberer et al., 2014; Li et al., 2011, 2014; Mao et al., 2010; Sun et al., 2002; Wang et al., 2011; Y. Yang et al., 2013; Zhao et al., 2009; Zhu et al., 2011). Contemporaneous Mo, Au and polymetallic mineralization took place and correlated well with these two stages (Cao et al., 2011; Chen et al., 2008; Li et al., 2012; Mao et al., 2011a,b; Stein et al., 1997, 2001; Wang et al., 2002; Y.

Yang et al., 2013), indicating a close association between metallogenesis and magmatism.

3. Geological characteristics of deposit

3.1. Ore zones and orebodies

The Zhaishang gold deposit is in the western Min–Li metallogenic belt in western Qinling Mountains, and lies within a regional brittle–ductile shear zone in the Zhuoluo–Zhamashu oblique anticline (Fig. 2). The inverted anticline has a north limb that dips between 45°N and 50°N, whereas the south limb dips between 60°N and 70°N. The spatial relation between the mineralized bodies and the anticline allows the deposit to be divided into a southern ore belt and a northern ore belt, which are located at the south and north sides of the anticline.

The ore deposit occurs both in rocks of low metamorphosed Middle Devonian and Lower Permian clastic formation, which is composed of quartz sandstone, siltstone, calcareous slate and argillaceous limestone.

More than 30 ore bodies have been delineated and these orebodies are rigorously spatially controlled both by faults and folds, such that the widths of host structural zones and the orebodies are basically identical. The orebodies are layered, bedded and lenticular in shape, and are

delineated mainly on the basis of geochemical data because the boundary between wall rock and orebody is not sharp.

The WNW-striking northern ore belt extends for more than 7200 m long and 1000 m wide, which is about 1200 m long and 300 m wide in our study area. This northern ore belt has nearly 20 mineralized veins (Fig. 2), which are present in the lower part of Lower Permian sandy slate, carbonaceous slate, calcareous slate and siltstone. The main orebodies are, from north to south, No. 19, No. 19-2, No. 19-1, No. 9, No. 10, No. 12, No. 11 and No. 21. These orebodies are subparallel and dip north between 20° and 60°. The distances between the northern orebodies are between 30 and 300 m. The proven resources in the north ore belt account for more than 80% of the proven resources of the entire mining area.

The Southern ore belt parallels the Northern ore belt and is more than 4200 m long and about 1000 m wide, which is about 1300 m long and 400 m wide in our study area. The ore belt has 6 mineralized veins, which are located in Middle Devonian rocks of argillaceous limestone, calcareous slate and silty slate. The main orebodies are, from north to south, No. 2, No. 42, No. 41, No. 32, No. 31, and No. 30 (Fig. 2). They are roughly subparallel with each other and the distances between them range from 200 to 300 m. No. 41 and No. 42 are north-dipping, with dips of 45° and 70°; No. 32 orebody is south-dipping, with dips between 50° and 75°; No. 31 is generally north-
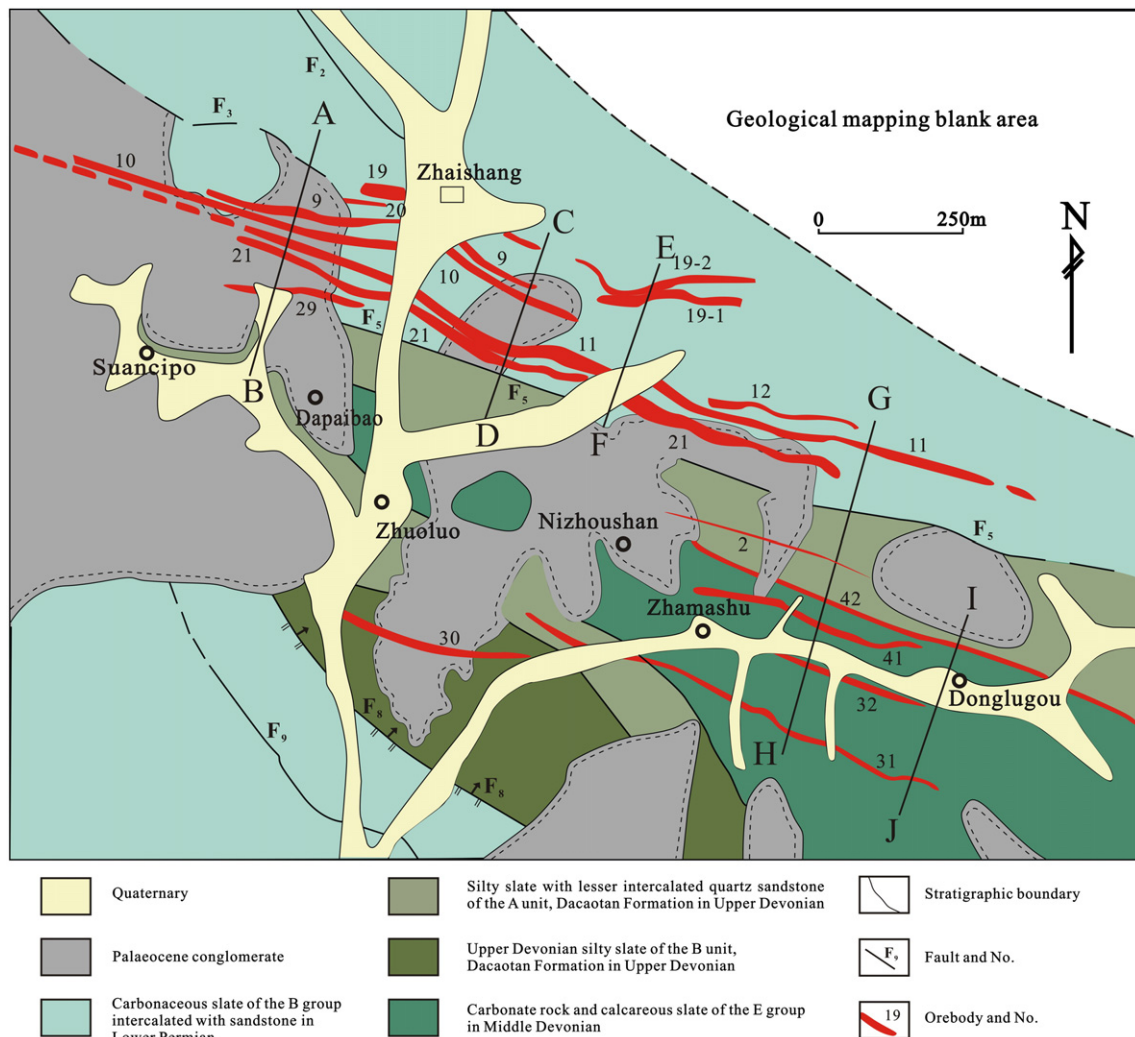

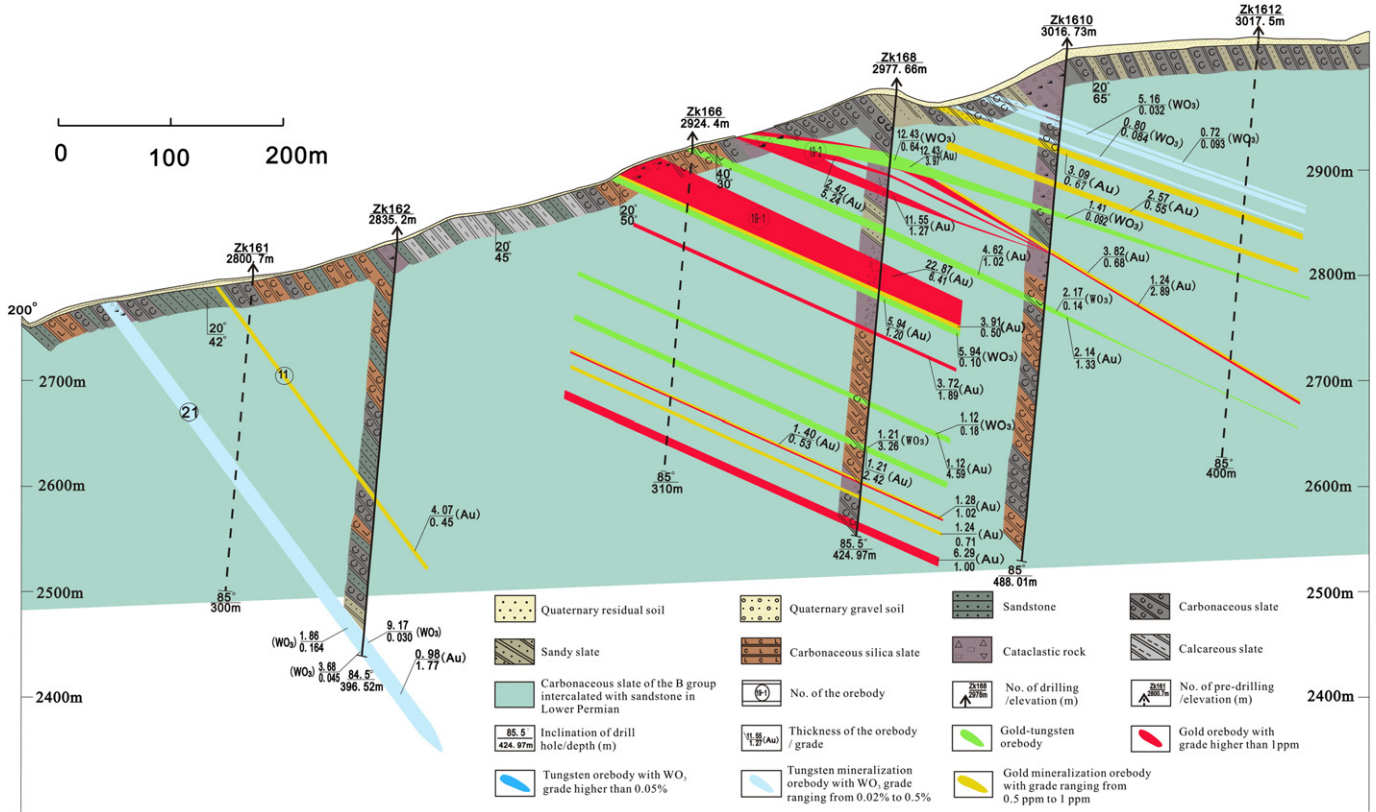**Fig. 2.** Simplified geologic map of the Zhaishang gold deposit. Modified after Liu et al. (2006).

Fig. 3. Geochemical section (Sections G–H) on prospection line 16 in the Zhaishang gold deposit.

dipping, however, in the ground surface to the east of Section I–J (Fig. 2), it appears to be south-dipping with dips between 55° and 90°, and in the deep part of this area it changes back to north dipping, with dips between 70° and 80°.

On the basis of chemical–analytical data, parts of the deposit can be delineated as independent scheelite orebodies (Fig. 3) characterized with the association Au–Sb–W (gold–scheelite–stibnite).

We carried out specific observations on No. 19, No. 19-2, No. 9, No. 10, No. 11 and No. 21 orebodies of the northern ore belt and No. 31, No. 32, No. 41 and No. 42 orebodies of the southern ore belt. Samples mentioned in this paper were taken from these orebodies.

3.2. Mineralogy

We have identified more than 40 minerals in the Zhaishang gold deposit (Table 2). Several sulfides, sulfosalts, oxides and oxysalt minerals are present, along with tellurides, elements, alloys, etc. In addition to most common minerals like pyrite, chalcopyrite, tetrahedrite, galena, sphalerite, stibnite, quartz, calcite, siderite, ankerite, rhodochrosite, and barite, rare minerals such as native gold (Fig. 4A, B, C), Cu–Zn–Ni–Sn–Fe alloys (Fig. 4D, E), as well as chalkostibite (Fig. 4F), bournonite (Fig. 4F), meneghinite (Fig. 4G), molybdenite (Fig. 4H), and scheelite

(Fig. 5) also are present. The complex ore mineral composition and the presence of microscopic visible natural gold constitute a major feature of the Zhaishang gold deposit.

Telluride minerals, such as coloradoite (Figs. 4A, C; 6A, B), melonite (Fig. 4A), petzite (Fig. 6B, C), muthmannite (Fig. 6B), and calaverite (Fig. 6B) (Liu et al., 2011b) also are characteristics of the Zhaishang gold deposit.

3.3. Ore texture and structure

The ore textures include: (1) framboidal texture (Fig. 7A); (2) euhedral–subhedral granular (Fig. 7B), anhedral granular (Fig. 7C), poikilitic (Fig. 7B), and mosaic textures formed as a result of crystallization; (3) metasomatic (Fig. 7C), metasomatic relict (Fig. 7C), pseudomorph, graphic textures or droplet-like, lattice, and grid filling textures resulting from metasomatism and filling; (4) colloidal (Fig. 7D), microscopic zonal textures (Fig. 7E) formed by colloidal processes; (5) rim texture (Fig. 7F); and (6) mortar (Fig. 7G), en-echelon double crystal (Fig. 7H) textures.

The ore structures include vein (Fig. 8A), network (Fig. 8B), comb (Fig. 8C), radiating (Fig. 8D), etc. A rough zoning with respect to ore structure (brecciation → network → veining), from early to late in

Table 2
Mineralogy of the gold ores in the Zhaishang gold deposit.

Type	Natural elements and alloys	Sulfide and sulfosalt minerals	Telluride	Oxide and oxygen-containing salts
Main		Pyrite, arsenopyrite, tetrahedrite, galena, stibnite		Quartz, calcite, scheelite, goethite, lepidocrocite
Minor	Native gold	Sphalerite, chalcopyrite, covellite, zinckenite, chalkostibite	Coloradoite, melonite	Ankerite, barite, gypsum, dickite, kaolinite azurite, malachite
Trace	Electrum, native copper, native nickel, Cu–Zn alloy, Cu–Zn–Ni–Sn–Fe alloy	Pyrrhotite, bournonite, molybdenite, gersdorffite, chalcocite, bornite, plagionite	Petzite, muthmannite, calaverite	Rhodochrosite, siderite, celestite, magnetite, hematite, rutile, cerusite
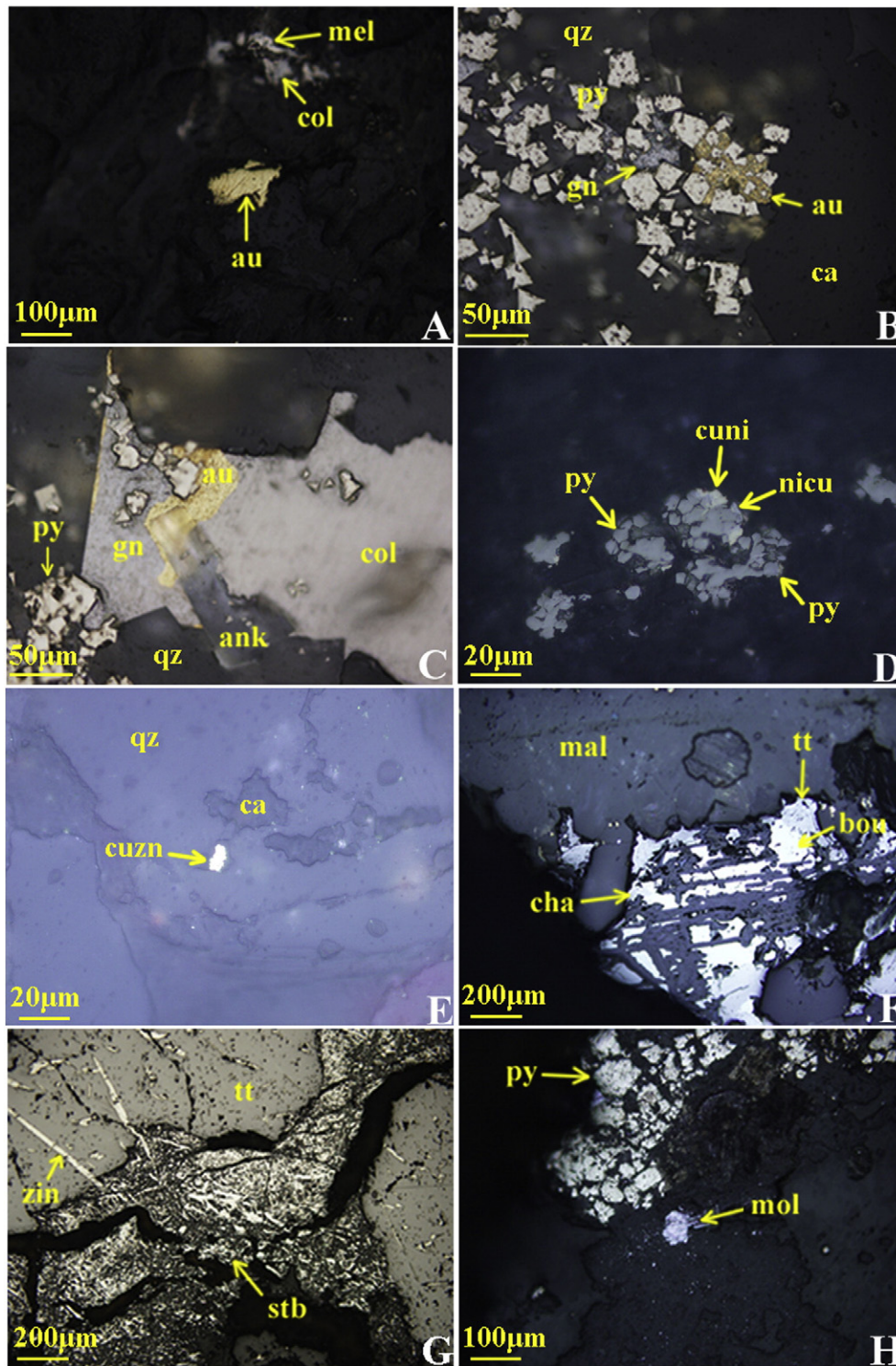
Fig. 4. Photomicrographs of some minerals from the gold ores in the Zhaishang gold deposit. All photomicrographs are in reflected light. Abbreviations: py = pyrite; tt = tetrahedrite; gn = galenite; stb = stibnite; mol = molybdenite; zin = zinckenite; cha = chalcostibnit; bou = bournonite; au = native gold; cuzn = Cu–Zn alloy; cuni =Cu–Ni alloy; nicu = Ni–Cu–Sn–Fe–Zn alloy; col = coloradoite; mel = melonite; mal = malachite; au = native gold; qz = quartz; ca = calcite; ank = ankerite.

turn, can be recognized from the center of the mineralization outwards in the tectonic fracture zone.

3.4. Ore types

According to the degree of oxidation, ores in the gold deposit can be divided into primary ores and oxidized ores.

The primary ores, the color of which varies from dark gray to light gray, generally are present within 40 m of the surface.

According to the characteristics of the original rocks, the primary ores have previously been divided into cataclastic carbonaceous ores, cataclastic silt-calcareous ores, cataclastic limestone ores, calcareous ores and strong silicified breccia ores (Lu et al., 2006). Local gold enrichments, some of economic interest, are also present in the Sb and W ores (Liu et al., 2008a).
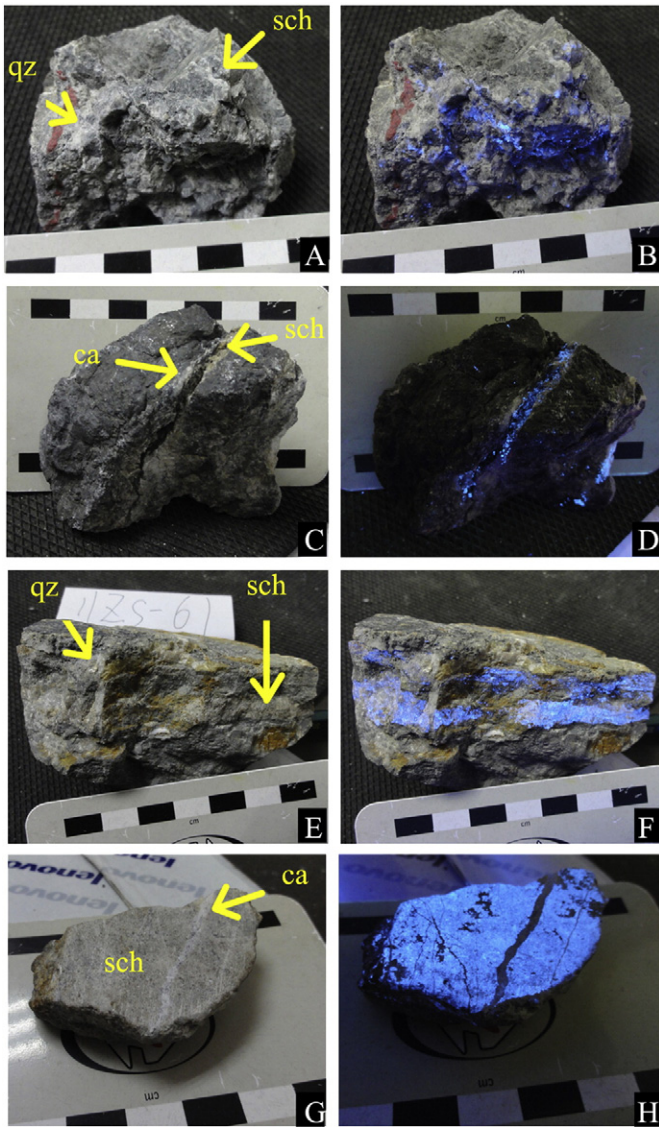
Fig. 5. Comparison photographs of the scheelite ore samples under natural light and UV light. A, C, E, and G. Scheelite is white with slightly yellow under natural light; B, D, F, and H. Scheelite glows bright blue fluorescent under UV light. A and B. Disseminated scheelite. C, D, E and F. Vein scheelite. G and H. Massive scheelite. Abbreviations: sch = scheelite; qz = quartz; ca = calcite.

The oxidized ores are brown and red-brown and generally present at the surface, roughly in the range of 0 to 40 m deep.

3.5. Wall-rock alteration

Alteration includes silicification, and the introduction of carbon, pyrite, stibnite, barite and kaolin. Gold mineralization, for the most part is most common where silica, carbon and pyrite are most intense.

Silicification is the most common hydrothermal alteration in the Zhaishang deposits and has developed in a number of paragenetic stages. There are two main types of silicification (Fig. 8A): type 1, planar distribution forming in fracture zones. The outstanding feature of silicification is that the color of the rocks turned from dark gray to light gray, or even grayish-white and organic matter is destroyed. Lithologic characteristics of silicified host rocks or ores are hard, dense, mostly light gray or gray; silicification type 2 is silica in veins or networks, which, in the early stage of hydrothermal mineralization, manifests as a vein

or thin layers filling in the brittle–ductile shear zone; in the middle stage of hydrothermal mineralization, it manifests as a thin vein filling along the micro-cracks of rocks or minerals; and in the late stage of hydrothermal mineralization, it manifests as a thin vein or network filling in the late broken belt. Generally, more intense silicification comes with better developed metal sulfide minerals, more complex ore components and more abundant gold mineralization, while a lack of silicification indicates poorly developed metal sulfide minerals and poor mineralization.

Pyrite introduction is a typical alteration type at Zhaishang. Pyrite was formed by hydrothermal activity (Fig. 4B, H). In addition, disseminated euhedral or subhedral pyrite occurs in micro-cracks, whereas subhedral, anhedral or sponge-textured pyrites are mostly present in brittle fracture zones. Fine-grained disseminated euhedral or subhedral pyrite is closely associated with gold mineralization (Fig. 4B, C), and is probably a positive correlation between the content of pyrite in ore and gold mineralization (Peters, 2004). The intensity of pyrite alteration directly reflects the degree of the gold mineralization.

Calcite and ankerite developed in late mineralization and are distributed in a limited area. They are mostly present in disseminations and veins and often found together with native gold particles.

Generally speaking, wherever wall-rock alteration is intensely developed, sulfide minerals and gold are abundant. Wherever wall-rock alteration is weak, sulfide minerals are less abundant and gold grades are lower.

3.6. Periods and stages of mineralization

The cross cutting and mineral assemblage features in the deposit suggest that mineralization processes of the Zhaishang gold deposit formed in three main intervals (Fig. 9): (1) sedimentary diagenesis, (2) syn-gold middle to low temperature hydrothermal mineralization and (3) post-gold supergene (Liu et al., 2008a,b; Ma et al., 2008). Based on the relationships of ore veins, mineral assemblages, paragenetic sequence (Fig. 9) and ore fabrics, five stages of mineralization in the syn-gold middle to low temperature hydrothermal period can be recognized:

(1) stage (I) is marked by low sulfide–quartz and is characterized by medium-to-fine-grained euhedral, subhedral pyrite and vein quartz. Pyrites are mostly 0.01 mm to 1 mm-sized middle to fine grained masses and disseminations within variably sized quartz veins and veinlets. Gold mineralization in this early stage is weak with Au concentrations of between 0.01 and 0.1 g/t.

(2) stage (II) is marked by arsenian pyrite–arsenopyrite–quartz and is characterized by small quartz veins, strong silicified zones, fine grained pyrite and arsenopyrite in the form of veins or dissemination. Pyrites, some of which have an overgrowth texture, are mostly smaller than 0.01 mm within or near the quartz veins with a crystal form of pentagonal dodecahedron (Fig. 7F, G). The arsenopyrites are smaller than 0.05 mm sized subhedral–euhedral spearhead-shaped, needle-shaped dissemination. Gold mineralization is intense with Au concentrations of between 1 and 5 g/t. In some intensely mineralized areas, Au concentrations could be higher than 10 g/t.

(3) stage (III) is marked by polymetallic sulfide–scheelite–quartz–carbonate and is characterized by various types of metal sulfide minerals such as pyrite, tetrahedrite, galena, chalcopyrite, sphalerite, stibnite, chalkostibite, zinckenite, bournonite, covellite, and molybdenite. Native gold and scheelite are commonly found. Gold mineralization in this stage is the most intense with Au concentrations of 5 g/t, up to 50 g/t.

(4) stage (IV) is marked by low sulfide–telluride–quartz–carbonate and is characterized by tellurides, ankerite, native gold, and other alloys. Galena, sphalerite and other sulfide minerals are
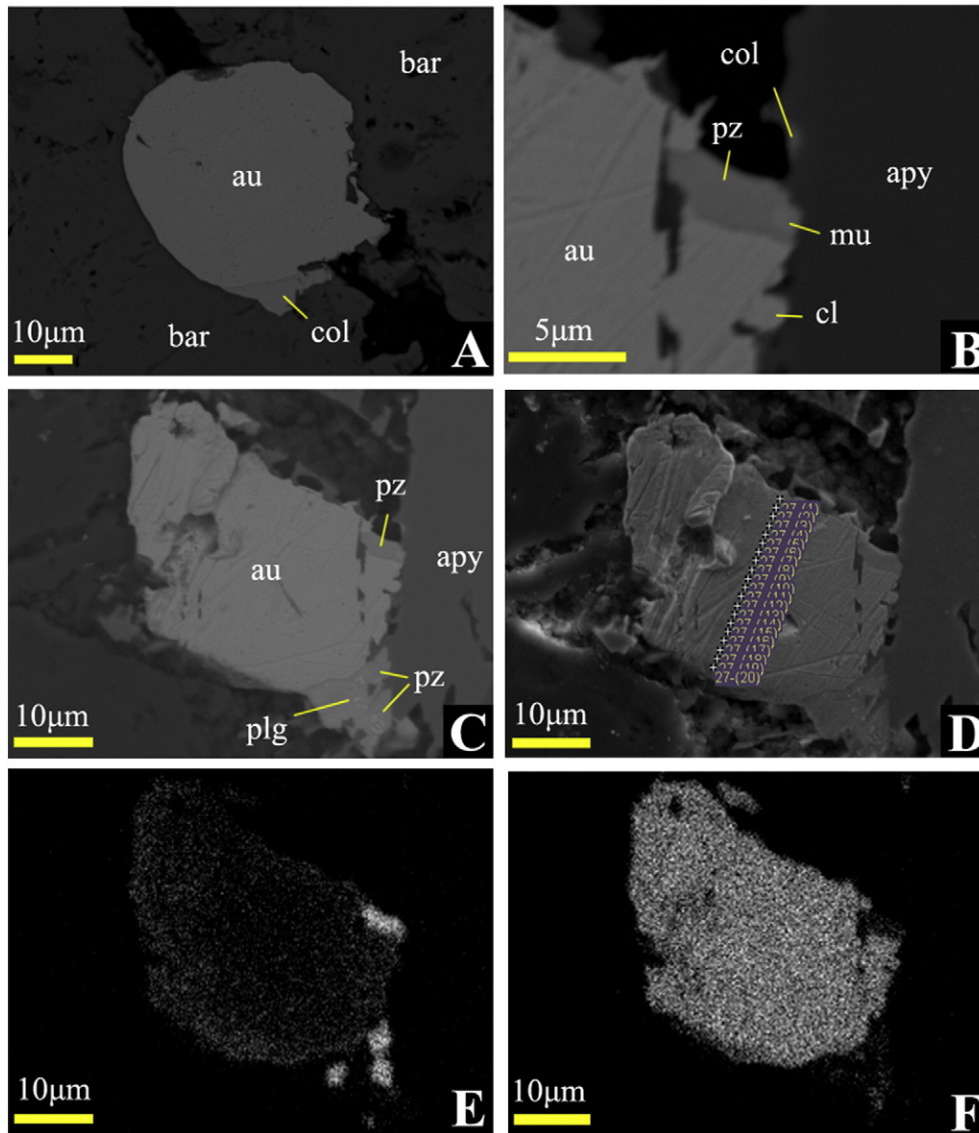
Fig. 6. The back-scattered electron, characteristic X-ray line scanning, X-ray line-by-line scanning images of native gold and some tellurides of the gold ores in the Zhaishang gold deposit. A–C. Back-scattered electron images. D. Characteristic X-ray line scanning image. E–F. X-ray scanning images of Au and Ag elements of native gold and petzite. Abbreviations: au = native gold; pz = petzite; mu = muthmannite; cl = calaverite; col = coloradoite; apy = arsenopyrite; plg = plagionite; bar = barite.

rarely seen. The Au concentrations of these ores are higher than 3 g/t.

(5) stage (V) is marked by carbonate–barite and is characterized by a large amount of carbonate veins, some quartz, barite, gypsum veinlets and weak metal mineralization. This stage is the last stage of hydrothermal mineralization. Gold mineralization is weak with Au concentrations lower than industrial grade.

Stage I is the pre-mineralization stage. Stages II, III and IV are the main stages. Stage V is the post-mineralization stage.

4. Geochemical methodology

Eighty-six samples of host rock, mineralized rock and ore samples were collected along the geological sections A–B, C–D, and G–H (Fig. 2), from exploration trenches, shallow pits, drill holes and from the orebodies. Firstly, thin, polished sections and double-polished inclusion sections were prepared. These were studied under the microscope to determine the extent of alteration, to investigate mineral assemblages, ore textures and inclusion characteristics. In accordance

with the microscopic observations. Selected samples were ground to −200 mesh. The selected ore minerals and gangue minerals were crushed, sieved and handpicked until grain size reached 40–60 mesh, and the purity exceeded 98 vol.%. Twenty-three samples of the ground quartz was then immersed in 5% dilute HNO_3 for 1 h to remove minor amounts of calcite. Finally, the pre-treated sample was repeatedly washed in clean and distilled water and then dried at 80 °C.

Various analyses and measurements were conducted on the selected samples. To determine the trace and rare earth element (REE) geochemistry of the deposit, ICP-MS analyses were conducted on the 86 rock, ore and hydrothermally-altered samples. Trace elements and REE contents were analyzed at the Laboratory of ICP-MS, Institute of Geophysical and Geochemical Exploration (IGGE). In order to estimate ore-formation temperature, the homogenization temperatures and salinities of fluid inclusions were measured by the senior author at the Laboratory of Ore Deposits, China University of Geosciences (Beijing) (CUGB). In order to constrain the sources of ore-forming material, various isotopic measurements were undertaken at the Stable Isotope Laboratory, Institute of Mineral Resources and Institute of Geology, Chinese
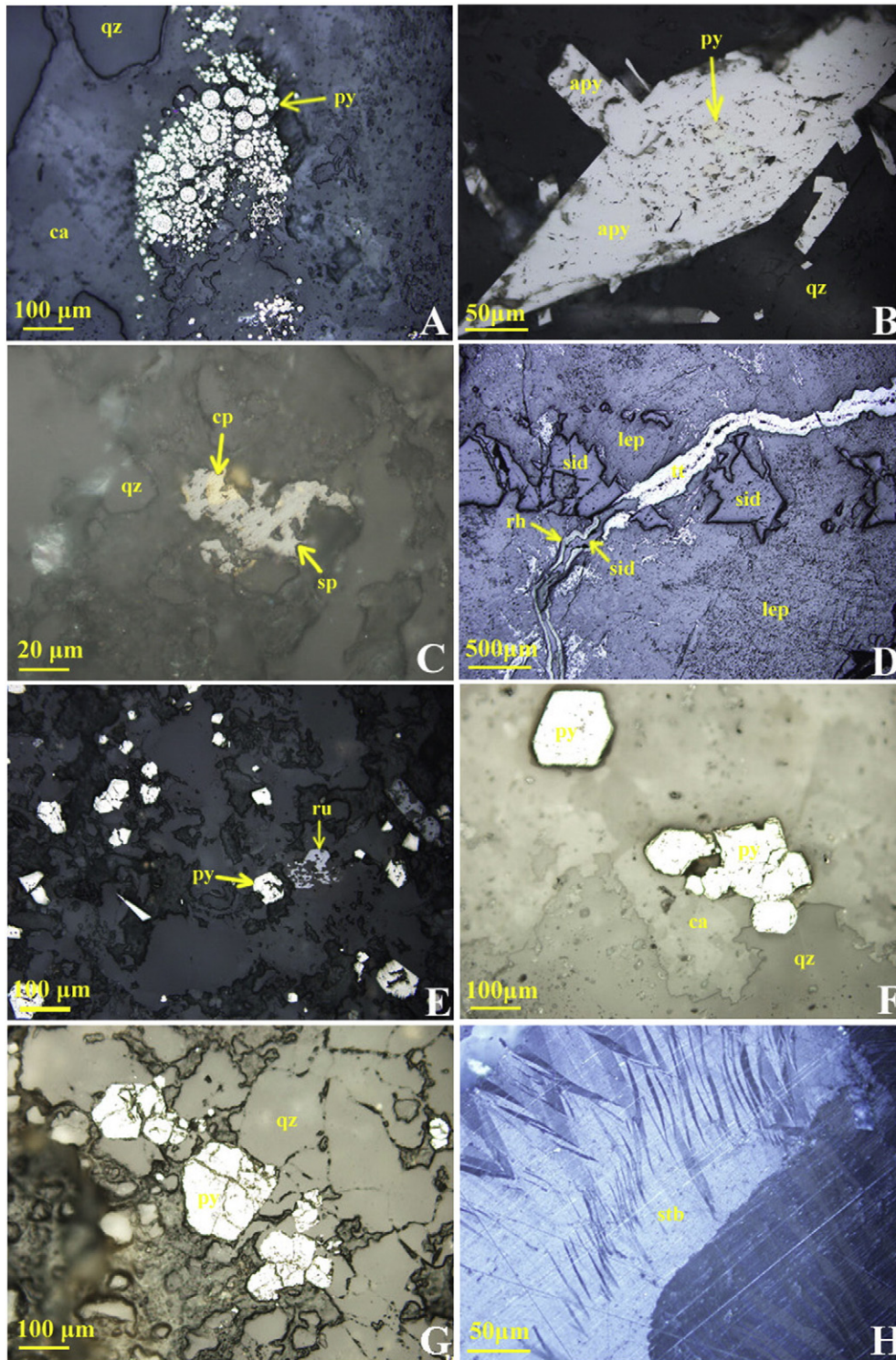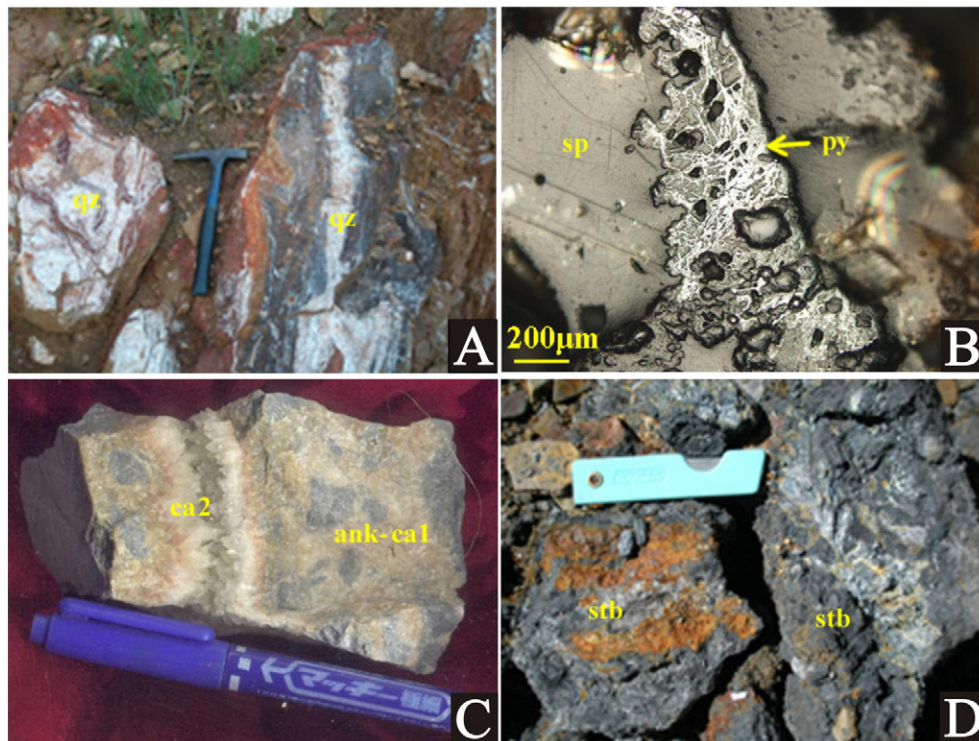
Fig. 7. Characteritic ore textures in the Zhaishang gold deposit. All photomicrographs are in reflected light. A. Abundant framboidal pyrite disseminated in carbonaceous slate type ores. B. Arsenopyrite, together with pyrite, constitute euhedral, subhedral and anhedral granular textures formed as a result of crystallization. C. Sphalerite replacing chalcopyrite. D. Rhodochrosite and siderite aggregate, showing colloidal texture. E. Microscopic girdle texture of pyrite in quartz. F. Ring fiber texture of pyrite in quartz. G. Cataclastic texture of pyrite in quartz. H. En echelon twins of stibnite. Abbreviations: apy = arsenopyrite; py = pyrite; cp = chalcopyrite; sp = sphalerite; stb = stibnite; sid = siderite; rh = rhodochrosite; lep = lepidokrocite; ru = rutile; qz = quartz; ca = calcite.

Academy of Geological Sciences (CAGS), at the Isotope Laboratory, Beijing Research Institute of Uranium Geology (BRIUG), and at the State Key Laboratory of Geological Processes and Mineral Resources, China University of Geosciences (GPMR). Analytical methods are described below.

For S-isotope analyses, Cu_2O was used as the oxidizer for the preparation of sulfide samples. Sulfate minerals were purified to pure $BaSO_4$ by the carbonate–zinc oxide semi-melt method, and then SO_2 was prepared by the V_2O_5 oxide method. VCDT standard material was used.

Fig. 8. Characteritic ore structures in the Zhaishang gold deposit. A. Quartz vein ore. B. Microscopic pyrite veinlet and stockwork ore in reflected light. C. Ankerite and calcite-cemented breccia ore, containing pectination structure of calcite. D. Stibnite massive and radiating ore; qz = quartz; py = pyrite; sp = sphalerite; ca = calcite; ank = ankerite; stb = stibnite.

For O and C isotope analysis, calcite and siderite were reacted with phosphoric acid at 25 °C (McCrea, 1950) to release CO_2. Two Chinese national standards of carbonate for C and O isotopes, GBW04416 and GBW04417, were used as working standards in experiments. The $\delta^{13}C_{PDB}$ and $\delta^{18}O_{PDB}$ values of GBW04416 determined by NBS-19 were 1.6 and −11.6‰, respectively. The $\delta^{13}C_{PDB}$ and $\delta^{18}O_{PDB}$ values of GBW04417 were −6.1 and −24.1‰, respectively. The $\delta^{18}O_{PDB}$ values of calcite samples were directly obtained from $\delta^{18}O$ values of their CO_2 against the CO_2 of PDB. To convert $\delta^{18}O_{PDB}$ to $\delta^{18}O_{SMOW}$, the equation by Friedman and O'Neil (1977) was used,

$$\delta^{18}O_{SMOW} = 1.03091 \times \delta^{18}O_{PDB} + 30.91.$$

For oxygen isotope analysis of silica and silicates, CO_2 was prepared by the BrF_5 method described by Clayton and Mayeda (1963). For H isotope analysis, the water in fluid inclusions was released by a decrepitation method. Then the water was reacted with Zn at 400 °C to produce H_2 (Coleman et al., 1982), which was collected in a sample tube with active charcoal at liquid N_2 temperature.

Silicon was extracted from samples by fluorination involving reaction with BrF_5 at 550 to 600 °C to produce SiF_4 gas (Ding et al., 1994). The SiF_4 gas was purified by liquid N_2 and dry ice–acetone separation; it was then passed through a preheated Cu tube containing pure Zn particles to remove any remaining BrF_5. The standard is NBS-28 quartz sandstone provided by the U.S. National Bureau of Standards and Technology. The measurements of quartz sandstone standard NBS-28 gave an average value of $\delta^{28}Si_{NBS-28} = 0.00 \pm 0.06‰$.

All SO_2, SiF_4, CO_2 and H_2 were analyzed in a Finnigan MAT-251 mass spectrometer and GV Multiflow-Isoprime mass spectrometer. Analytical precision was ±0.15‰ for C, O, and S isotopes, ±0.1‰ for Si isotopes, and ±2‰ for H isotopes.

For Pb isotope analysis, we used the sample pre-treatment procedure described by Robin et al. (1999). Pyrite, galena, tetrahedrite and stibnite (400 mg) were first washed with HCl to remove impurities coated on the mineral surfaces, then dissolved in aqua regia under heating, and finally converted to a HBr chromatographic solution. The Pb in solution was eluted using an ion exchange resin with HBr-HCl. 13 samples were used for analysis on a MAT-261 mass spectrometer. Of the samples, 20% was repeatedly analyzed. The fractionation factor (0.1% per amu) is worked out in terms of the results of Pb isotopic analyses of NBS-981 as the international standard, so as to make correlations for the Pb isotopic ratios of the samples. Measurements of common-lead standard NBS-981 gave average values of $^{206}Pb/^{204}Pb = 16.923 \pm 3$, $^{207}Pb/^{204}Pb = 15.467 \pm 3$, $^{208}Pb/^{204}Pb = 36.733 \pm 6$ for VG-354 and $^{206}Pb/^{204}Pb = 16.924 \pm 3$, $^{207}Pb/^{204}Pb = 15.468 \pm 3$, $^{208}Pb/^{204}Pb = 36.732 \pm 6$ for MAT-261 with uncertainties <0.1% at the 95% confidence level. The bulk lead blanks for the whole procedure are <1 ng and analytical results for all samples are corrected for this. Duplicate analysis indicates similar reproducibility in all cases. The bulk error is <0.1% for lead isotopic samples.

5. Results

5.1. REE geochemistry

Because the chondrite-normalized REE distribution patterns of most samples share a number of common features, the authors selected the ICP-MS results of some representative samples for discussion. Chondrite-normalized REE distribution patterns are shown in Table 3 and Fig. 10. Analytical results indicate that, in various kinds of low Ca-bearing sedimentary rocks (Fig. 10A, B), siltstone and carbonaceous slate have high ΣREE (110.09 ppm–249.57 ppm, mostly exceeding 180.00 ppm), high LREE/HREE ratios (5.57–11.27) with slopes $(La/Yb)_N$ of 6.20 to 11.36, a greater extent of LREE fractionation $[(La/Sm)_N = 3.37–4.43]$ than that of HREE fractionation $[(Tb/Yb)_N = 1.10–1.68]$, significant negative Eu anomalies (δEu = 0.40–0.72) and weak negative Ce anomalies (δCe = 0.82–0.95). However, the sedimentary rocks containing high calcium (calcareous slate, calcareous sandstone) have low ΣREE (91.63 ppm–135.28 ppm), high LREE/HREE ratios (7.87–9.39) with slopes $(La/Yb)_N$ of 8.34 to

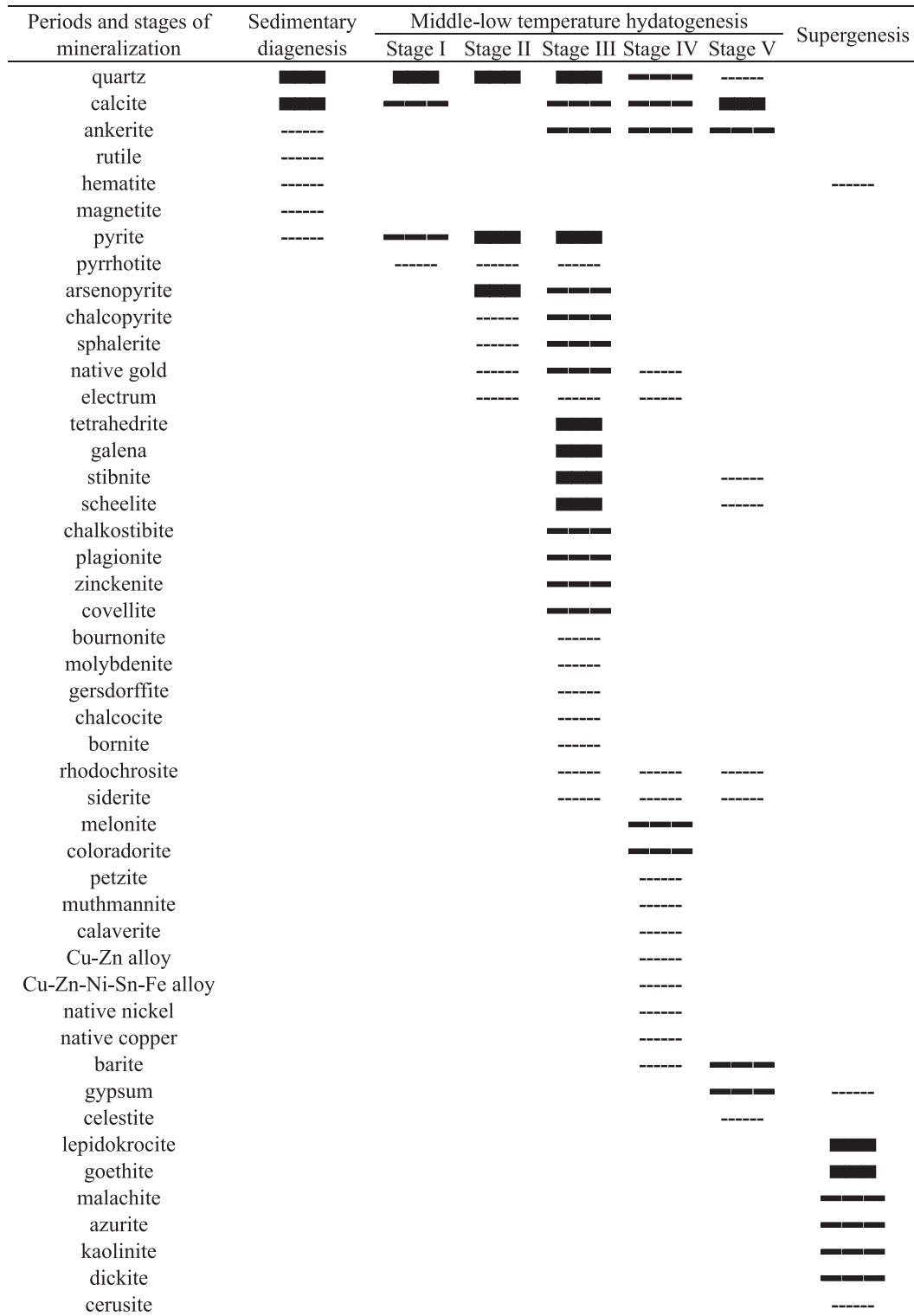| Periods and stages of mineralization	Sedimentary diagenesis	Middle-low temperature hydatogenesis					Supergenesis
		Stage I	Stage II	Stage III	Stage IV	Stage V	
quartz	▬	▬	▬	▬	▬	------	
calcite	▬	▬		▬	▬	▬	
ankerite	------			▬	▬	▬	
rutile	------						
hematite	------						------
magnetite	------						
pyrite	------	▬	▬	▬			
pyrrhotite		------	------	------			
arsenopyrite			▬	▬			
chalcopyrite			------	▬			
sphalerite			------	▬			
native gold			------	▬	------		
electrum			------	------	------		
tetrahedrite				▬			
galena				▬			
stibnite				▬		------	
scheelite				▬		------	
chalkostibite				▬			
plagionite				▬			
zinckenite				▬			
covellite				▬			
bournonite				------			
molybdenite				------			
gersdorffite				------			
chalcocite				------			
bornite				------			
rhodochrosite				------	------	------	
siderite				------	------	------	
melonite					▬		
coloradorite					▬		
petzite					------		
muthmannite					------		
calaverite					------		
Cu-Zn alloy					------		
Cu-Zn-Ni-Sn-Fe alloy					------		
native nickel					------		
native copper					------		
barite					------	▬	
gypsum						▬	------
celestite						------	
lepidokrocite							▬
goethite							▬
malachite							▬
azurite							▬
kaolinite							▬
dickite							▬
cerusite							------

Fig. 9. Paragenetic sequence of main minerals from the periods and stages of mineralization. Width of lines corresponds to the relative abundance of minerals of each stage.

12.16, a greater extent of LREE fractionation [$(La/Sm)_N$ = 3.85–4.30] than that of HREE fractionation [$(Tb/Yb)_N$ = 1.30–1.61], obvious negative Eu anomalies (δEu = 0.72–0.86) and very weak negative Ce anomalies (δCe = 0.82–0.93). Two limestone samples' ΣREE (30.70 ppm–72.10 ppm), LREE/HREE ratios (3.76–5.86) and slopes $(La/Yb)_N$ of 3.92 to 7.39 are all lower than those of other sedimentary rocks, and although the extent of LREE fractionation [$(La/Sm)_N$ = 2.79–3.77] is greater than

that of HREE fractionation [$(Tb/Yb)_N$ = 1.28–1.39], the difference between them is far less significant than that of other sedimentary rocks. The Eu anomalies of limestone (δEu = 0.68–1.01) vary greatly from obviously negative to normal, but the Ce anomalies (δCe = 0.72–0.87) are obviously negative.

Ores (Fig. 10C) and hydrothermal minerals (Fig. 10D) have distinctly different REE distribution patterns. Ores have high ΣREE

Table 3

REE compositions of the host rocks, ore and single mineral samples in the Zhaishang gold deposit (ppm).

Sample No.	06ZS-3	06ZS-16	06ZS-18	06ZS-27	06ZS-29	06ZS-40	06ZS-73	06ZS-11	06ZS-69	S06ZS-7	06ZS-75	06ZS-2	06ZS-35	06ZS-1	06ZS-10
Sample name	Siltstone				c	Arbonaceous slate				Calcareous slate		Calcareous sandstone	Silicated sandstone	Limestone	
La	47.3	28.1	54.9	24.7	34.4	43.8	39.9	42.1	27.6	28.9	20.4	31.1	26.7	7.3	14.0
Ce	88	49	108	45	65	71	74	78	49	53	37	51	51	10	23
Pr	10.82	6.18	12.98	5.67	8.24	9.99	9.37	9.37	6.59	6.90	4.53	7.00	5.87	1.55	2.99
Nd	38.6	21.5	44.5	19.7	29.3	34.5	33.6	32.9	23.7	25.0	15.9	24.6	20.7	5.8	12.2
Sm	7.16	3.99	7.94	3.82	5.71	6.48	6.52	6.32	5.14	4.73	3.11	4.55	3.60	1.21	3.16
Eu	1.57	0.54	1.41	0.73	0.71	1.41	1.06	0.92	1.06	1.18	0.82	1.00	0.80	0.27	1.17
Gd	6.24	4.02	5.77	3.51	5.04	5.61	5.40	5.52	5.82	4.39	2.73	3.97	3.22	1.22	3.98
Tb	1.01	0.70	0.86	0.56	0.86	0.89	0.88	0.90	1.07	0.71	0.46	0.63	0.49	0.21	0.70
Dy	5.58	3.89	4.88	2.84	5.01	4.76	4.85	5.10	5.65	3.94	2.47	3.32	2.45	1.20	4.02
Ho	1.11	0.77	1.06	0.51	1.04	0.94	0.97	1.02	1.02	0.81	0.50	0.63	0.47	0.26	0.82
Er	3.24	2.15	3.19	1.46	3.00	2.63	2.85	2.92	2.79	2.28	1.41	1.79	1.33	0.70	2.39
Tm	0.56	0.37	0.57	0.25	0.54	0.46	0.52	0.54	0.51	0.41	0.26	0.30	0.23	0.11	0.42
Yb	3.34	2.17	3.43	1.47	3.33	2.81	3.04	3.16	3.00	2.34	1.56	1.72	1.30	0.66	2.42
Lu	0.57	0.37	0.58	0.25	0.57	0.47	0.50	0.54	0.50	0.38	0.26	0.29	0.21	0.11	0.41
ΣREE	214.62	123.23	249.57	110.09	162.45	185.97	183.08	189.32	133.80	135.28	91.63	131.46	118.05	30.67	72.12
LREE/HREE	8.91	7.54	11.27	9.15	7.38	9.01	8.64	8.61	5.57	7.87	8.49	9.39	11.18	5.86	3.76
(La/Yb)$_N$	9.54	8.74	10.78	11.36	6.97	10.49	8.86	8.98	6.20	8.34	8.81	12.16	13.90	7.39	3.92
(La/Sm)$_N$	4.16	4.43	4.35	4.08	3.79	4.25	3.85	4.19	3.37	3.85	4.12	4.30	4.67	3.77	2.79
(Tb/Yb)$_N$	1.33	1.42	1.10	1.68	1.14	1.40	1.28	1.26	1.57	1.34	1.30	1.61	1.67	1.39	1.28
δEu	0.72	0.41	0.64	0.61	0.40	0.72	0.55	0.48	0.59	0.79	0.86	0.72	0.72	0.68	1.01
δCe	0.93	0.89	0.97	0.91	0.92	0.82	0.92	0.95	0.88	0.91	0.93	0.82	0.97	0.72	0.87

Table 3 (continued)

| Sample No.	06ZS-46	06ZS-23	S06ZS-56	06ZS-62	06ZS-58	06ZS-78	06ZS-14	06ZS-71	06ZS-77	06ZS-17	06ZS-21	S06ZS-41	06ZS-53	06ZS-36	06ZS-39	06ZS-13	06ZS-52
Sample name	Carbonaceous slate		Calcareous slate ores	Mineralized sandstone	Mineralized breccia		Carbonaceous slate ores			Oxidized ores		Pyrite	Tetrahedrite	Quartz	Stibnite		Calcite
La	29.5	22.7	37.6	48.0	44.2	35.8	45.3	37.6	26.8	37.9	44.5	25.2	3.1	5.7	7.8	25.6	4.2
Ce	57	44	70	87	87	60	80	66	51	82	83	49	3	23	17	17	3
Pr	6.49	5.36	8.45	10.82	10.51	7.83	10.51	8.55	6.39	9.99	9.99	5.97	0.41	1.65	2.16	2.06	0.52
Nd	23.1	19.3	29.8	37.6	37.2	27.3	37.9	30.1	23.0	35.5	35.2	23.6	1.6	6.2	9.3	8.3	2.0
Sm	4.74	4.05	5.47	7.04	7.02	4.91	7.45	5.68	4.76	6.84	6.64	5.53	0.35	1.34	4.16	4.10	0.65
Eu	1.30	0.95	1.38	1.35	1.52	1.00	1.03	1.09	0.88	1.23	1.52	3.50	0.12	0.39	1.31	1.68	0.26
Gd	4.61	4.00	4.30	6.56	6.35	4.30	6.47	5.09	4.60	5.71	6.08	7.97	0.33	1.40	5.39	7.82	0.82
Tb	0.70	0.74	0.61	1.02	1.02	0.71	1.05	0.84	0.78	0.88	1.01	1.27	0.04	0.21	1.05	1.24	0.14
Dy	3.45	4.25	3.01	5.01	5.71	3.89	5.83	4.47	4.22	4.79	5.49	6.37	0.21	1.20	5.60	6.24	0.87
Ho	0.61	0.85	0.60	0.90	1.13	0.76	1.15	0.87	0.81	0.95	1.07	1.12	0.04	0.25	0.97	0.98	0.17
Er	1.60	2.37	1.84	2.43	3.25	2.19	3.36	2.47	2.20	2.75	2.98	2.81	0.11	0.78	2.42	2.03	0.46
Tm	0.26	0.43	0.35	0.41	0.57	0.39	0.59	0.41	0.37	0.49	0.50	0.44	0.02	0.15	0.40	0.28	0.09
Yb	1.52	2.49	2.21	2.36	3.33	2.31	3.51	2.44	2.25	2.86	2.91	2.46	0.12	0.93	2.28	1.29	0.54
Lu	0.25	0.44	0.38	0.39	0.55	0.38	0.58	0.40	0.38	0.48	0.46	0.41	0.02	0.16	0.35	0.19	0.09
ΣREE	134.80	112.30	166.00	210.65	209.17	151.62	204.62	165.90	128.32	192.64	201.46	135.23	9.33	43.30	59.85	78.54	13.40
LREE/HREE	9.36	6.21	11.48	10.04	8.55	9.15	8.08	8.76	7.22	9.19	8.83	4.92	9.48	7.53	2.24	2.91	3.22
(La/Yb)$_N$	13.06	6.13	11.50	13.71	8.94	10.42	8.71	10.40	8.04	8.94	10.30	6.89	16.96	4.16	2.31	13.37	5.17
(La/Sm)$_N$	3.92	3.52	4.33	4.29	3.96	4.58	3.83	4.17	3.55	3.49	4.21	2.86	5.68	2.69	1.18	3.92	4.03
(Tb/Yb)$_N$	2.03	1.31	1.22	1.90	1.35	1.35	1.32	1.52	1.53	1.36	1.53	2.27	1.42	1.00	2.03	4.24	1.14
δEu	0.85	0.72	0.87	0.61	0.70	0.67	0.45	0.62	0.57	0.60	0.73	1.61	1.09	0.87	0.85	0.91	1.09
δCe	0.98	0.97	0.94	0.92	0.97	0.86	0.88	0.88	0.94	1.02	0.95	0.95	0.60	1.80	0.98	0.56	0.44
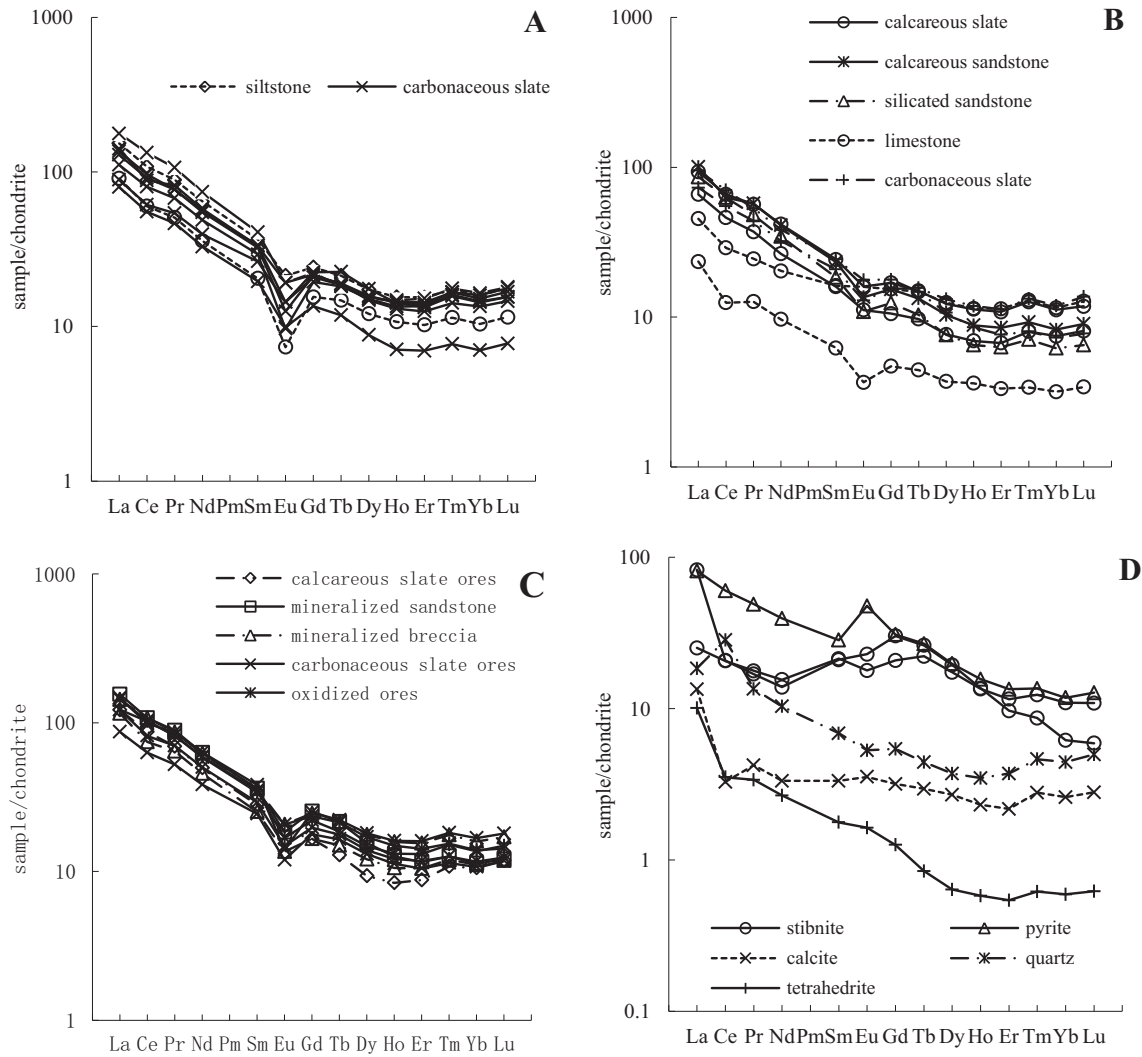
Fig. 10. Chondrite-normalized REE pattern of rocks, ores and hydrothermal minerals in the Zhaishang gold deposit.

(128.32 ppm–210.65 ppm), high LREE/HREE ratios (7.22–11.48) with slopes $(La/Yb)_N$ of 8.04 to 13.71, a greater extent of LREE fractionation $[(La/Sm)_N = 3.49–4.58]$ than that of HREE $[(Tb/Yb)_N = 1.22–1.90]$, obvious negative Eu anomalies $(\delta Eu = 0.45–0.87)$ and weak negative and unremarkable Ce anomalies $(\delta Ce = 0.86–1.02)$. These features are substantially the same with those of carbonaceous slate and siltstone, reflecting that the REE distribution characteristics of ore is inherited from those of the host rock.

The ΣREE of hydrothermal minerals (pyrite, tetrahedrite, quartz, stibnite and calcite) (9.33 ppm–78.54 ppm) is relatively low, with only a few samples' ΣREE reaching to 135.23 ppm. In accordance with their mineralization stages, the samples can be divided into three groups (Fig. 10D).

Samples of the first group (pyrite, tetrahedrite and quartz) display strong LREE enrichment (LREE/HREE = 4.92–9.48). For this group of samples, the extent of LREE fractionation $[(La/Sm)_N = 2.69–5.68]$ is greater than that of HREE $[(Tb/Yb)_N = 1.00–2.27]$, and Ce, Eu both display moderate negative anomalies to strong positive anomalies $(\delta Ce = 0.60–1.80, \delta Eu = 0.87–1.61)$. These above features reflect that reaction occurred between the ore-forming fluid and the wall rock.

Samples of the second group (stibnite) display enrichment of the HREE, low LREE/HREE ratios (2.24–2.91) with largely various slopes $(La/Yb)_N = 2.31–13.37$, and moderate or weak Ce depletion and Eu

depletion. The extent of LREE fractionation of this group is weaker $[(La/Sm)_N = 1.18–3.92]$ than that of HREE fractionation $[(Tb/Yb)_N = 2.03–4.24]$. These features may be related to the dissolution of calcium minerals and gypsum in the host rock. Gypsum is a calcium mineral, and calcium ion radius is equivalent to the ion radius of MREE, resulting in the enrichment of MREE (Liu et al., 1984). Therefore, the material source of those hydrothermal minerals with such REE distribution patterns is closely related to ore-bearing rock.

Sample of the third group (calcite) displays a flat or nearly flat REE distribution pattern. The LREE/HREE ratio is 3.22 with slope $(La/Yb)_N$ of 5.17. For this group, the extent of LREE fractionations $[(La/Sm)_N = 4.03]$ is greater than that of HREE $[(Tb/Yb)_N = 1.14]$. Ce is strongly depleted $(\delta Ce = 0.44)$ and Eu displays positive anomaly $(\delta Eu = 1.09)$. The formation of minerals with such REE characteristics may be associated with magmatic activity such as diabase and diorite veins which were recently found in the mining area, revealing fluid from deep sources joining the ore-forming processes.

5.2. Isotope geochemistry

5.2.1. Sulfur isotopic compositions

The hydrothermal sulfides in the Zhaishang gold deposit are mainly pyrite, stibnite, tetrahedrite and galena. Sulfates are gypsum and barite.

Table 4
$\delta^{34}S$ values of major sulfides from the in the Zhaishang gold deposit.

Seq. No.	Sample no.	$\delta^{34}S_{-CDT}$ (‰)								Stages of minieralization
		Arsenopyrite	Pyrite	Tetrahedrite	Galena	Sphalerite	Stibnite	Barite	Gypsum	
1	06ZS-175		32.37							Sedimentary diagenesis
2	06ZS-89		27.75							
3	06ZS-102	5.57								Stage II
4	06ZS-104		7.95							Stage II
5	06ZS-105		7.61							Stage II
6	06ZS-174		9.69							Stage III
7	06ZS-18		8.60							Stage III
8	06ZS-23		7.54							Stage III
9	06ZS-73		10.32							Stage III
10	06ZS-51			2.23						Stage III
11	06ZS-52			1.35						Stage III
12	06ZS-53				0.20					Stage III
13	06ZS-80				10.24					Stage III
14	06ZS-80					2.31				Stage III
15	06ZS-13						4.92			Stage III
16	06ZS-32						7.41			Stage III
17	06ZS-3						1.47			Stage III
18	06ZS-34								0.55	Stage V
19	06ZS-51							13.23		Stage V
20	ZS12		4.50							
21	ZS52		7.50							
22	ZS53		9.20							
23	ZS64-2-1		3.70							
24	ZS64-2-2		3.10							
25	ZS33		7.50							
26	ZS64-2				3.20					
27	ZS18						3.00			

Note: Sequence Nos. 1–19 samples were analyzed at the Isotope Laboratory, Beijing Research Institute of Uranium Geology (BRIUG); data for the others were published by Lu et al. (2006).

A small amount of sedimentary–diagenetic pyrite can also be seen in ore-bearing stratum. The sulfur isotopic compositions of 27 sulfide and sulfate samples (Table 4, Fig. 11), including 8 samples from Lu et al. (2006), show that the $\delta^{34}S$ values vary from 0.20 to 32.37‰, averaging 7.87‰, without an obvious tower-shaped distribution.

Two sedimentary–diagenetic pyrite samples have high $\delta^{34}S$ (27.75‰, 32.37‰), close to or exceeding the $\delta^{34}S$ values of Devonian sea water (20‰–25‰, Claypool et al., 1980). Therefore, the $\delta^{34}S$ values of sedimentary–diagenetic pyrites are very similar to the $\delta^{34}S$ values

of the sulfide minerals formed in a shallow closed sea environment (Ohmoto, 1972; Ohmoto and Rye, 1979).

The $\delta^{34}S$ values of 25 sulfide samples formed in the hydrothermal mineralization is relatively low (Fig. 11). The $\delta^{34}S$ value range of pyrite is 3.10‰ to 10.32‰ (average on 7.26, n = 12), while stibnite is 1.47‰ to 7.41‰ (average on 4.20, n = 4), galena 0.20‰ to 10.24‰ (average on 4.55, n = 3), arsenopyrite 5.57‰ (n = 1), sphalerite 2.31‰ (n = 1), and tetrahedrite 1.35‰ to 2.23‰ (average on 1.79, n = 2). The $\delta^{34}S$ values of gypsum (n = 1) and barite (n = 1) formed by hydrothermal activity are also low (0.55‰ and 13.23‰, respectively), which is rare in a hydrothermal deposit. So far, in the Zhaishang gold deposit, we haven't found the close coexistence of sulfide minerals, gypsum, and barite in the main mineralization stage, which indicates that a certain group of sulfur clusters (H_2S or SO_4^{2-}) dominates in ore-forming fluid, so the sulfur isotope composition of these minerals can represent the isotopic composition of total sulfur in hydrothermal fluid (Liu et al., 2000b). Therefore, the range of $\delta^{34}S$ values of hydrothermal sulfides basically represents the characteristics of total sulfur of the hydrothermal fluid, meaning that the average $\delta^{34}S$ value (5.61‰) of hydrothermal sulfides can approximately represent the $\delta^{34}S_{\Sigma S}$ of ore-forming fluid. Obviously, the $\delta^{34}S$ values of total sulfur of a hydrothermal fluid are significantly lower than those of sedimentary–diagenetic pyrites in the study area and higher than those of magmatic or mantle sulfur. On one hand, it may indicate the mixing of sulfur from the stratum and sulfur from the magma; on the other hand, it may be related to the variation of temperature, pH and fO_2 when those minerals are formed.

Generally speaking, when sulfur exchange in hydrothermal fluid reaches equilibrium, the $\delta^{34}S$ values of major sulfur minerals should follow the fractionation order of $\delta^{34}S_{arsenopyrite} > \delta^{34}S_{pyrite} > \delta^{34}S_{pyrrhotite} > \delta^{34}S_{stibnite}$ (Ohmoto and Rye, 1979). However, sulfur isotopic compositions of sulfide samples in the deposit may not follow this fractionation order (taking into account that there is only one arsenopyrite sample), indicating that sulfur isotopes in various minerals have not reached equilibrium, which is consistent with the phenomenon of boiling happening in the ore-froming fluid (Ma et al., 2008).
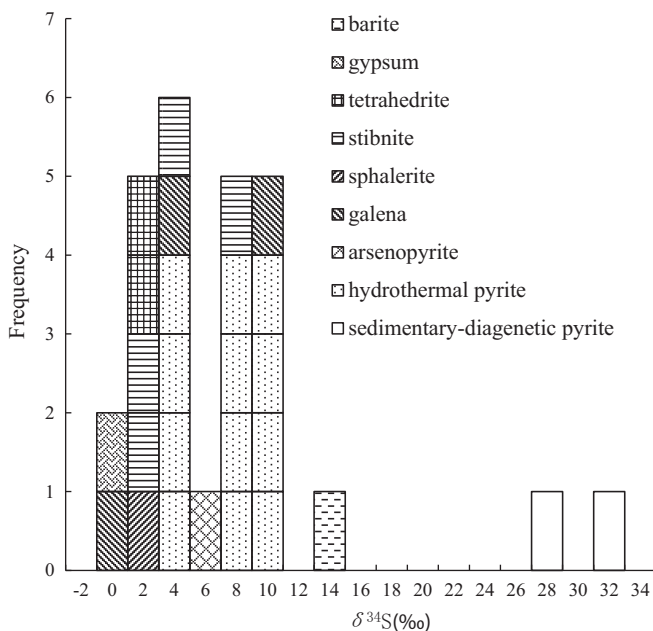

Fig. 11. Sulfur isotope distribution in the Zhaishang gold deposit.

Table 5
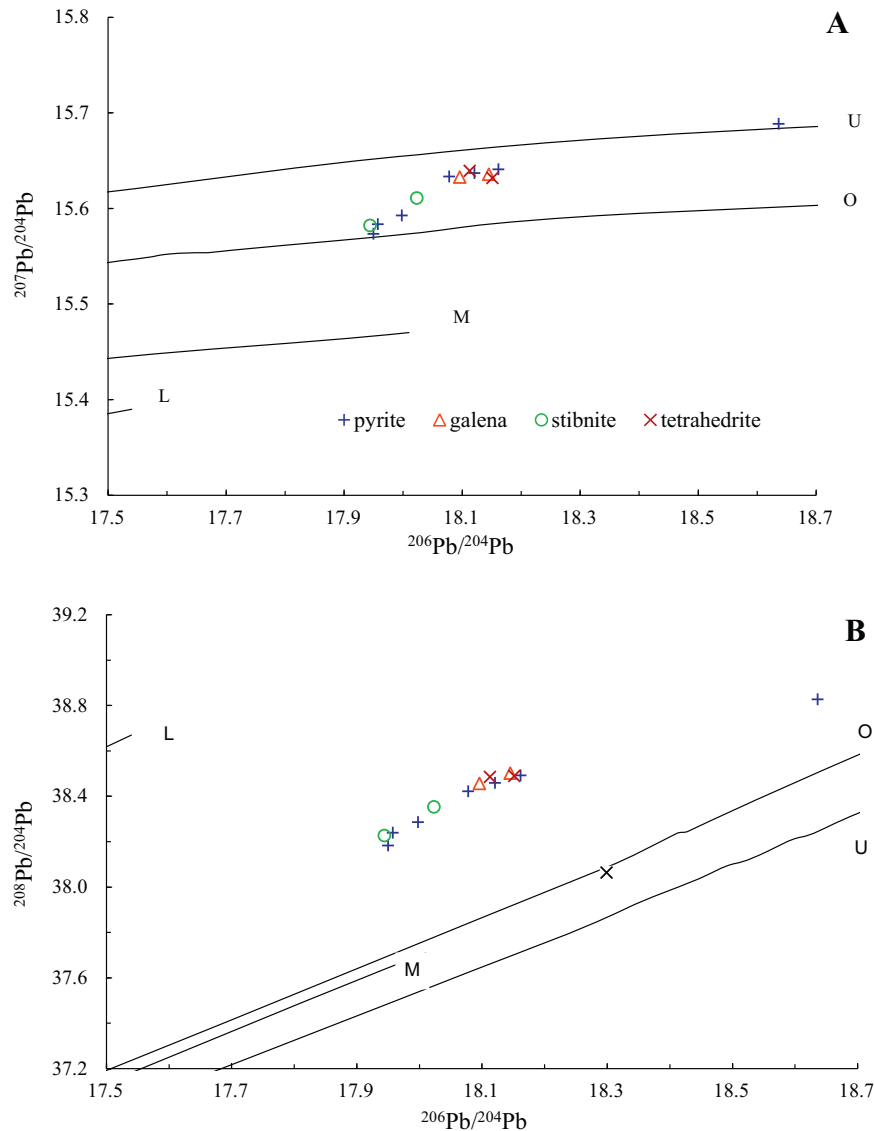Pb isotopic compositions of the rocks and hydrothermal minerals from the gold deposit.

Seq. No.	Sample No.	Mineral and rock	$^{206}Pb/^{204}Pb$ (2σ)	$^{207}Pb/^{204}Pb$ (2σ)	$^{208}Pb/^{204}Pb$ (2σ)
1	06ZS-18	Pyrite	38.2855 (29)	15.5927 (11)	17.9978 (14)
2	06ZS-73	Pyrite	38.1826 (21)	15.5733 (7)	17.9501 (9)
3	06ZS-74	Pyrite	38.2385 (34)	15.5836 (11)	17.9573 (11)
4	06ZS-75	Pyrite	38.4579 (25)	15.6370 (11)	18.1209 (12)
5	06ZS-89	Pyrite	38.4204 (45)	15.6335 (18)	18.0780 (21)
6	06ZS-101	Pyrite	38.4906 (14)	15.6410 (6)	18.1618 (7)
7	06ZS-102	Pyrite	38.8267 (19)	15.6883 (7)	18.6364 (8)
8	06ZS-53	Galena	38.5004 (17)	15.6356 (7)	18.1455 (8)
9	06ZS-80	Galena	38.4553 (49)	15.6327 (19)	18.0960 (20)
10	06ZS-13	Stibnite	38.2255 (21)	15.5822 (8)	17.9443 (9)
11	06ZS-32	Stibnite	38.3522 (14)	15.6109 (5)	18.0235 (5)
12	06ZS-51	Tetrahedrite	38.4888 (25)	15.6317 (10)	18.1517 (12)
13	06ZS-52	Tetrahedrite	38.4845 (25)	15.6392 (10)	18.1130 (11)

Note: All samples were analyzed at the Stable Isotope Laboratory, Institute of Geology, Chinese Academy of Geological Sciences (CAGS); data in the brackets are analytical errors (2σ).

5.2.2. Lead isotopic compositions

Pb isotopic compositional analyses were performed on sulfide minerals such as pyrite (n = 7), galena (n = 2), stibnite (n = 2), and tetrahedrite (n = 2). Ore lead isotopic compositions are rather uniform (Table 5), as evidenced by the Pb isotopic ratios: $^{206}Pb/^{204}Pb$ = 17.9443 to 18.1517; $^{207}Pb/^{204}Pb$ = 15.5733 to 15.6392; $^{208}Pb/^{204}Pb$ = 38.1826 to 38.5004. Their rates of change are 1.16%, 0.42% and 0.83%. But the single-stage model ages of ores (391 to 481 Ma) vary in a narrow

Fig. 12. Lead isotopic compositions of the Zhaishang deposit. Zartman's lead evolution model (Doe and Zartman, 1979; Zartman and Doe, 1981): M = upper mantle lead; O = orogenic belt lead; U = upper crustal lead; L = lower crustal lead.

Table 6
Carbon, oxygen and hydrogen isotopic compositions of quartz, calcite and siderite.

Seq. No.	Sample No.	Mineral	$\delta^{13}C_{PDB}$ (‰)	$\delta^{18}O_{SMOW}$ (‰)	$\delta^{18}O_{H2O\text{-}SMOW}$[a] (‰)	δD_{SMOW}[b] (‰)	Th[c] (°C)	Stages of mineralization
1	06ZS-31	Quartz		20.70	15.48	−91	372	Stage I
2	06ZS-24	Quartz		20.90	13.25	−90	293	Stage II
3	06ZS-68	Quartz		22.00	13.85	−93	280	Stage II
4	06ZS-39	Quartz		20.50	5.54	−88	162	Stage III
5	06ZS-9	Calcite	−0.43	18.52	10.37	−81	230	Stage III
6	06ZS-48	Calcite	−0.09	19.36	9.67	−73	198	Stage III
7	06ZS-28	Calcite	−2.04	17.63			192	Stage III
8	06ZS-82	Calcite	−0.36	19.18			255	Stage III
9	06ZS-15	Quartz		21.00	7.86	−95	186	Stage IV
10	06ZS-81-1	Calcite	−0.27	19.38	6.69	−74	150	Stage IV
11	06ZS-42	Calcite	−0.15	18.27			211	Stage IV
12	06ZS-81-2	Quartz		21.10	7.53	−82	180	Stage V
13	06ZS-37	Siderite	−2.08	19.89	9.11	−99	190	Stage V
14	06ZS-49	Calcite	0.02	19.63	7.36	−75	156	Stage V
15	06ZS-44	Calcite	0.85	19.60				Stage V
16	06ZS-105	Calcite	3.93	17.48	7.88	−96	200	Stage V
17	06ZS-106	Calcite	1.05	18.02	8.44	−85	200	Stage V
18	ZS12	Quartz		15.80	4.21	−65	210	
19	ZS14	Quartz		19.80	8.21	−69	210	
20	ZS15	Quartz		20.00	8.41	−72	210	
21	ZS53	Quartz		20.70	9.11	−76	210	
22	ZS63	Quartz		21.30	9.71	−92	210	
23	ZS64-2	Quartz		20.20	8.61	−90	210	
24	ZS65	Quartz		20.50	8.91	−77	210	
25	ZS66	Quartz		22.10	10.51	−74	210	
26	ZS67	Quartz		19.90	8.31	−81	210	

Note: The carbon isotopic compositions of Sequence Nos. 1–17 samples were analyzed at the State Key Laboratory of Geological Processes and Mineral Resources, China University of Geosciences (GPMR). The oxygen and hydrogen isotopic compositions of Sequence Nos. 1–17 samples were analyzed at the Stable Isotope Laboratory, Institute of Mineral Resources, Chinese Academy of Geological Sciences (CAGS); data for the others were published by Lu et al. (2006).

[a] Calculated based on the equations $1000\ln\alpha_{quartz\text{-}water} = 3.38 \times 10^6 \, T^{-2} - 2.90$ (Friedman and O'Neil, 1977), $1000\ln\alpha_{calcite\text{-}wate} = 2.78 \times 10^6 \, t^{-2} - 2.89$ (O'Neil et al., 1969), and $1000\ln\alpha_{siderite\text{-}water} = 2.88 \times 10^6 \, T^{-2} - 2.70$ (O'Neil and Silberman, 1974) using filling temperatures of fluid inclusions in quartz (Th).

[b] Water from fluid inclusions in quartz, siderite, and calcite.

[c] Filling temperatures of fluid inclusions.

range, mainly in the range of 400–460 Ma, indicating that the metallogenic material stems are possibly derived from the ore-bearing stratum itself or the underlying formation.

To characterize the tectonic environment of the source region of ore lead, the Pb isotope data from various ore lenses have been plotted against the different evolutionary curves relative to Pb plumbotectonic models. As can be seen from the $^{207}Pb/^{204}Pb$–$^{206}Pb/^{204}Pb$ diagram (Fig. 12A) and the $^{208}Pb/^{204}Pb$–$^{206}Pb/^{204}Pb$ diagram (Fig. 12B), the data of all samples fall near the upper crust and the orogenic Pb evolutionary curves, and show a good linear relationship with high correlation coefficients between $^{207}Pb/^{204}Pb$ and $^{206}Pb/^{204}Pb$ (R = 0.9570),

between $^{208}Pb/^{204}Pb$ and $^{206}Pb/^{204}Pb$ (R = 0.9843), indicating that the source of Pb (and Au) is from the upper crustal rocks.

5.2.3. Carbon isotopic compositions

Calcite is one of the most common gangue minerals in the Zhaishang gold deposit. The results of C and O isotope analysis for hydrothermal calcite in ore is given in Table 6. As can be seen from the Table 6, $\delta^{13}C_{PDB}$ values show little variation from −2.04 to +3.93‰ (on average +0.25‰), but $\delta^{18}O_{SMOW}$ values are highly variable from +17.48 to +19.63‰ (on average +18.71‰). It is well known that the range of $\delta^{13}C$ values of marine carbonate is very small (−1 to +2‰, on average 0‰, Keith and Weber, 1964), and the $\delta^{18}O$ values are generally higher than 20‰; the $\delta^{13}C$ values of deep igneous carbonate and diamond are concentrated in the range of −7 to −2‰; $\delta^{18}O$ values of magmatic
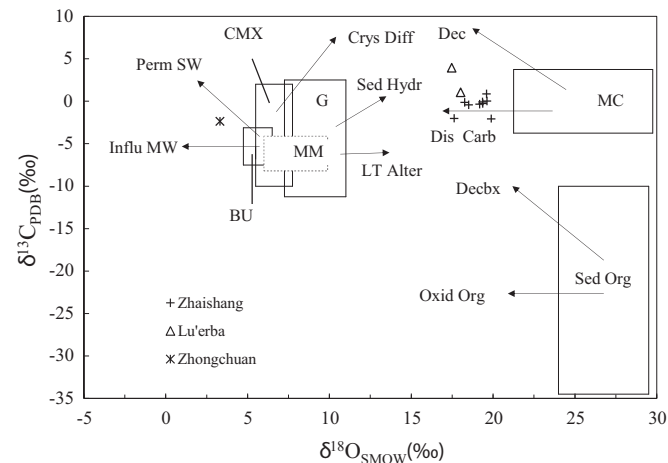
Fig. 13. $\delta^{18}O$ versus $\delta^{13}C$ diagram of calcite and siderite from the Zhaishang gold deposit. After Liu and Liu (1997) and Liu et al. (2004).

Table 7
$\delta^{30}Si$ values of the rock and ore-forming quartz veins from the Zhaishang gold deposit.

Seq. No.	Sample No.	Mineral and rock	$\delta^{30}Si_{\text{-}NBS\text{-}28}$ (‰)
1	06ZS-15	Quartz	−0.2
2	06ZS-24	Quartz	−0.4
3	06ZS-31	Quartz	−0.3
4	06ZS-39	Quartz	−0.7
5	06ZS-68	Quartz	−0.7
6	06ZS-81	Quartz	−0.3
7	06ZS-32	Siltstone	−0.3
8	06ZS-76	Silty sandstone	−0.3
9	06ZS-13	Calcareous sandstone	−0.5
10	06ZS-2	Carbonaceous slate	−0.3
11	06ZS-56	Calcareous slate	−0.2
12	11ZS-67	Diabase	0.1
13	11ZS-68	Diorite	0.2

Note: Samples were analyzed at the Stable Isotope Laboratory, Institute of Mineral Resources, Chinese Academy of Geological Sciences (CAGS).

hydrothermal fluid are between 5.0‰ and 10.5‰. Based on the data given above, $\delta^{13}C$ and $\delta^{18}O$ values of the Zhaishang gold deposit are between those of marine carbonate and those of deep-source carbonate, and obviously different from those of calcites in the Zhongchuan granite ($\delta^{13}C = -2.37‰$, $\delta^{18}O = 3.32‰$, Wang and Chen, 2002) in the same region (Fig. 13).

As can be seen from the $\delta^{18}O$–$\delta^{13}C$ diagram (Fig. 13), the data of hydrothermal calcites mainly fall near the left side of the marine carbonate area. This pattern suggests the source of C&O in the vein may have been derived from marine carbonate in the host rocks.

In addition, the range of $\delta^{13}C$ values is very small, and the $\delta^{18}O$ values are between 11.40‰ and 19.84‰, therefore the plotted data are horizontally distributed in general. There could be two reasons for this: (1) degasification of CO_2; and (2) the water–rock interaction between the fluid and wall rocks (Liu et al., 2004; Zheng, 1990; Zheng and Hoefs, 1993). If the distribution of the carbon and oxygen isotopes was mainly affected by the degasification of CO_2, the impact would be significant on the carbon isotope but not on the oxygen isotope, because the hydrothermal fluid is mainly composed of H_2O. However, the range of $\delta^{13}C$ values is very small, therefore the degasification of CO_2 could not have been the main factor which affected the precipitation of calcite. In the hydrothermal fluid, the solubility of calcite increases with the decrease of temperature, and decreases with the decrease of pressure. In a closed system, calcite cannot precipitate from the fluid only by cooling (Zheng, 2001). So the precipitation of calcite in the deposit was probably caused by the coupling of water–rock interaction and decrease of temperature.

5.2.4. Silica isotopes

Silicon isotope analysis was performed on 7 hydrothermal quartz and 6 whole rock samples, the latter including chert, siltstone, slate and a diabase dyke. The $\delta^{30}Si$ values (Table 7) of hydrothermal quartz in the deposit lie within the range -0.7 to $-0.2‰$. Such values are more negative than those ($+0.1$ to $+0.2‰$) of diorite and diabase dyke in the mine district but are similar to those of ore-hosting siltstones, calcareous sandstone, calcareous slate, silty sandstone and carbonaceous slates (-0.5 to $-0.2‰$).

Available studies (Fitoussi et al., 2009; Huang et al., 2010) have shown that the variation of $\delta^{30}Si$ values is controlled by Si isotope dynamic fractionation. The first precipitated silica has the lowest $\delta^{30}Si$ value. With an increasing proportion of precipitated silica, $\delta^{30}Si$ values will increase steadily to a large, positive value (Ding et al., 1994). Studies by Clayton (1986) also indicate that when SiO_2 is leached out of the rocks by hydrothermal solutions, Si isotope fractionation will not generally take place. However, when SiO_2 is precipitated from hydrothermal solutions, $\delta^{30}Si$ fractionation between precipitated SiO_2 and the residual SiO_2 in the hydrothermal solutions will occur, but to varying degrees. If temperatures of hydrothermal solutions are relatively high (>300–400 °C), SiO_2 will be rapidly and completely precipitated, and such Si isotope fractionation mentioned above would be negligible. In contrast, if temperatures are relatively low (<300–400 °C), SiO_2 will be precipitated slowly and incrementally, and $\delta^{30}Si$ values of SiO_2 will be accordingly low. Formation temperatures of the Zhaishang deposit are mainly in the range 120–240 °C, so the sedimentary ($\delta^{30}Si = -0.5$ to $-0.2‰$) and volcanic rocks ($\delta^{30}Si = +0.1$ to $+0.2‰$) in this region may have provided some silica for the ore-forming fluids.

5.2.5. Hydrogen and oxygen isotopic compositions of fluid inclusions

A total of 11 quartz, calcite and siderite samples were analyzed for $\delta^{18}O$ of the host minerals and δD values of fluid from fluid inclusions, and our study also quoted the data analyzed by Lu et al. (2006). Results are shown in Table 6. The $\delta^{18}O$ values of fluids are calculated from the $\delta^{18}O$ of quartz, calcite and siderite based on the equations $1000\ln\alpha$ (quartz–water) = $3.38 \times 10^6\,T^{-2} - 2.90$ (Friedman and O'Neil, 1977), $1000\ln_{calcite–wate} = 2.78 \times 10^6\,t^{-2} - 2.89$ (O'Neil et al., 1969) and $1000\ln\alpha$ (siderite–water) = $2.88 \times 10^6\,T^{-2} - 2.70$ (O'Neil and

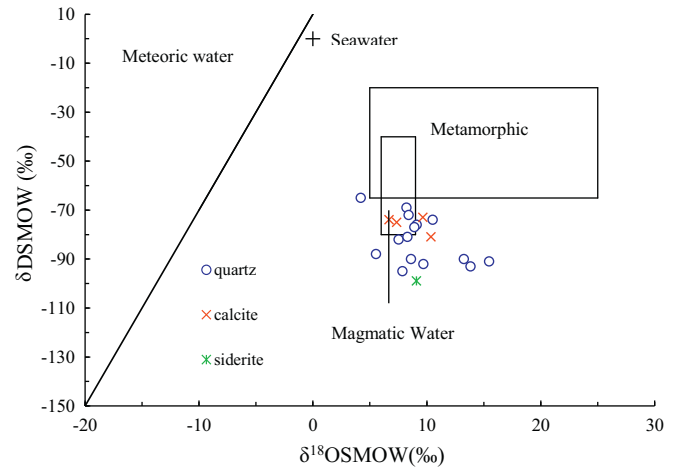**Fig. 14.** $\delta^{18}O$ versus δD diagram of fluid inclusions of the Zhaishang gold deposit. Modified after Sheppard (1986).

Silberman, 1974) using filling temperatures of fluid inclusions in quartz (Th). The δD values of fluids were directly taken from the measurements from fluid inclusions.

The $\delta^{18}O$ and δD values of ore-forming fluids vary, respectively, from $+4.71$ to $+14.42‰$ and from -99 to $-73‰$ for the main stage of mineralization. These ranges are consistent with some typical Carlin-like gold deposit in this region, such as Jinlongshan ($\delta^{18}O = +4.1‰$ to $+13.7$, $\delta D = -105$ to $-63‰$, Zhang et al., 2002a,b), Manaoke ($\delta^{18}O = +1.04‰$ to $+12.11‰$, $\delta D = -100.7$ to $-57.9‰$, Wang et al., 2004), Yangshan ($\delta^{18}O = +3.7‰$ to $+12.2‰$, $\delta D = -92.4$ to $-56‰$, Yu et al., 2010), Shuangwang ($\delta^{18}O = -0.78$ to $15.84‰$, $\delta D = -103.9$ to $-60.0‰$, Liu et al., 2011a), and Baguamiao ($\delta^{18}O = -3.07$ to $13.30‰$, $\delta D = -117.9$ to $-53.38‰$, He et al., 2009).

In order to explore the properties of ore-forming fluids, all data were projected onto a diagram of hydrogen and oxygen isotopic composition for various types of water (Fig. 14). It can be seen that the data for most of the samples fall outside the areas of typical magmatic or metamorphic waters, and a few fall in the area of magmatic water, indicating that the ore-forming fluid were derived predominantly from a groundwater (meteoric waters) system. Samples mostly plot below or near the lower right side of the magmatic area, at a great distance from the meteoric water line. This so-called "$\delta^{18}O$ shift" reflects a high degree of O isotope exchange in water–rock interaction between meteoric water and rock (Liu et al., 2000b, 2007). However, generally speaking, when the exchange took place between ore-forming fluid and rocks, the water/rock ratio was relatively insignificant, and the exchange water had relatively stable $\delta^{18}O$ values but variable δD values. Therefore, data plotted in Fig. 10 show the trend of vertical distribution.

5.3. Fluid inclusion characteristics and estimation of ore-formation temperature

The petrography and geochemistry of fluid inclusions in the Zhaishang gold deposit has been reported in detail by Ma et al. (2008). On the basis of field observation and laboratory analysis in recent years, we select samples formed in different mineralization stages, and new results are briefly introduced as follows.

5.3.1. Fluid inclusion characteristics

There are a large number of fluid inclusions in quartz and calcite, which are related to the mineralization. The fluid inclusions vary greatly in shape. Inclusions in quartz are mostly elliptical, rounded and irregular in shape while inclusions in calcite are mostly rectangular, rhomb-
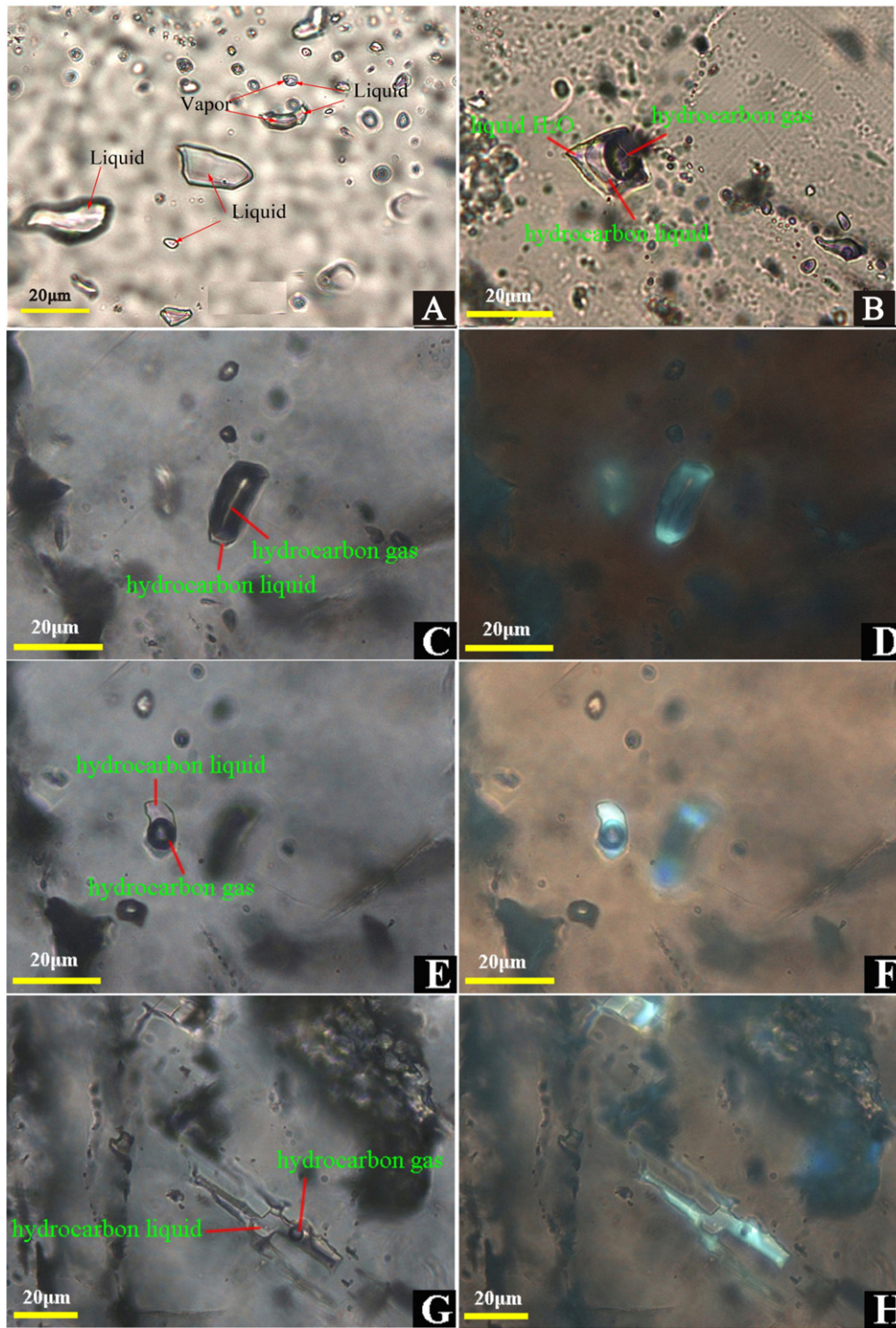
Fig. 15. Photomicrographs of hydrocarbon fluid inclusions from barite in the Zhaishang gold deposit. A. Pure liquid inclusion and two-phase vapor–liquid inclusion. B. Three-phase inclusion containing aqueous liquid and an immiscible liquid hydrocarbon surrounding the vapor bubble, under transmitted light. C, E, G. Two-phase hydrocarbon inclusion, under transmitted light. D, F, H. The same field of view as part (C), (E) and (G), respectively, showing the hydrocarbon fluid inclusions under incident UV light.

shaped and triangular. The inclusions are isolated, in groups or string beaded (without cutting through the host mineral) distributed, 3–25 μm in size. In primary inclusions, the water part is mostly colorless and transparent, and the color of the vapor phase varies slightly due to the different compositions of the inclusions. The bubbles in the salt–water inclusion were mainly colorless and transparent, but sometimes gray or grayish black because of the refraction or the total reflection of light by the bubble wall.

According to the types of phase state and the temperature of transformation point, two major types of fluid inclusions have been distinguished: (1) aqueous-solution two-phase inclusions are all composed of water and vapor, of which vapor accounts for 5 to 20% of the total volume. They are widespread developed in the gangue minerals and account for 80%–90% of the total number of fluid inclusions. They are mostly colorless, and 2 μm to 25 μm in size. A few of them are nearly composed of pure liquid and coexist with two-phase inclusions. There

are also a few elliptical, rounded and irregular-shaped gas-rich inclusions, which are below 8 μm in size, with the vapor accounting for above 60% of the total volume and of relatively dark color. When heating, the vapor phase disappears and homogenizes to liquid. (2) CO_2-rich three-phase inclusions are composed of liquid CO_2, gaseous CO_2 and liquid H_2O, of which CO_2 accounts for 5 to 12% of the total inclusion volume. They are commonly found in quartz grains but the quantity is relatively small. They coexist with aqueous solution two-phase inclusions, and are mostly negative crystal shaped, elliptical or irregular shaped. When heated, CO_2 disappears in most cases and homogenizes to an aqueous solution; some inclusions decrepitate before reaching homogenization.

It is worth noting that we found a small number of three-phase inclusions which contains hydrocarbons in the fifth mineralization stage (Fig. 15). These inclusions are elliptical and trapezoid, 10–20 μm in size. These three-phase inclusions, consisted of aqueous–salt solution, liquid hydrocarbon and hydrocarbon gas, with immiscibility between water and oil, are mostly found in barite vein. The vapor phase was black and brown with weak fluorescence effect or no fluorescence. The liquid hydrocarbon was colorless or light-brown and have light blue-white to blue-white fluorescence effect. The salt solution was colorless and have no fluorescence effect. The existence of hydrocarbon inclusions in the Zhaishang deposit indicates that there once was movement of hydrocarbon fluid, which may be related to the carbonaceous shale stratum of Devonian and Permian in this area. There are only two causes for the existence of organic gas in geothermal systems: these are microbiological action and the pyrolysis of kerogen in sedimentary rock (Welhan, 1988). Previous researches suggest that organic matter could affect metal mineralization in four ways: complexation, adsorption, exchange of cation and reduction (Sun et al., 2001). The chemical reaction between organic fluid and ore-forming fluid may have been beneficial to the precipitation of metallogenic material in the carbonaceous shale stratum.

5.3.2. Physical and chemical conditions of mineralization

The authors systematically measured homogenization temperatures, salinities and densities of inclusions in hydrothermal minerals such as quartz, calcite, ankerite and barite. The homogenization temperatures are 105–372 °C (Table 8 and Fig. 16), with salinities of 0.70 to 23.11 wt.%, densities of 0.71 to 1.03 g/cm^3 and pressures of 23.8 to 78.1 MPa. From the early to late stages of mineralization, temperature and pressure of ore-forming fluid have gradually decreased. In the main ore-forming stages (II, III, IV), the temperatures vary greatly, but mainly in the range of 120–240 °C. The salinity of ore-forming fluid is middle to low. The salinity of main ore-forming stages (II, III, IV) is higher than that of the early (I) and late (V) stages. Especially in the low sulfide–telluride–quartz–carbonate main stage (IV), the salinity is up to 25.95 wt.% with the average value higher than the other two main ore-forming stages (II, III). The density of ore-forming fluids range from 0.71 to 1.03 g/cm^3, centralizing at 0.85–0.98 g/cm^3.

Due to the coexistence of different phase fluid inclusions, the fact that during the measurement of the homogenization temperature, when the inclusions reach homogenization, some of them homogenize to vapor phase (Ma et al., 2008), and the appearance of negative correlation between homogenization temperatures and salinities in part of the inclusions, there is a great possibility that the Zhaishang gold deposit had experienced fluid boiling or phase separation during mineralization stages.

5.3.3. The composition of ore-forming fluid

The results of our studies (Table 9) of compositions of both vapor phase and liquid phase in fluid inclusions indicate that principal cations in ore-forming fluid are Na^+ and Ca^{2+}, secondly K^+, and rarely Mg^{2+}, with $Na^+/K^+ > 1$ and $Na^+/(Ca^{2+}+Mg^{2+}) = 0.5$ to 2.0. Anions are mostly Cl^- and SO_4^{2-} with some NO_3^{2-} and few F^-, and the content of Cl^- and SO_4^{2-} are tens or hundreds of times higher than that of the rest of the anions. The content of SO_4^{2-} and Cl^- in different ore veins is variable and shows different ascendancies. Despite H_2O, the vapor phase is chiefly composed of CO_2, N_2 and CH_4, with a small amount of hydrocarbons like C_2H_2, C_2H_4 and C_2H_6, which is consistent with the results of the Laser Raman Work (Ma et al., 2008). Based on the calculation of the composition of the vapor phase, the parameters of oxidation and reduction concentrate in the range of 0.004 to 0.044 (nm). Thus the ore-forming fluid can be represented by the "salt solution–CO_2–CH_4" hydrothermal system.

6. Ore-forming mechanism

The study of geochemistry, stable isotopic compositions, and fluid inclusion characteristics of the Zhaishang gold deposit shows that the ore-forming hydrothermal fluid was derived from heated recycling groundwater recharged by meteoric water, rich in organic matter, and possibly mixed with fluid from a deep source being associated with magmatic activity. Tectonic thermal effects and geothermal gradient were the two main factors that activated and drove the fluid. The carbonaceous shale stratum of Devonian and Permian with a high gold content laid the foundation both for the preconcentration of gold and the material exchange between ore-forming fluid and sedimentary basin rocks. The unique tectonic setting played a positive role in ore formation. The tectonic deformation provided not only heat, but also plenty of suitable space for later mineralization. After having full material exchange with basin sediments the ore-forming fluid migrated to structurally deformed zones, and at the same time, because of the mixing of different kinds of fluid (heated cycling ore-bearing hot brine, organic-rich fluid and possible magmatic water) and the sudden drop of the confining pressure, the gold metallic sulfides precipitated and enriched.

The Zhaishang gold deposit had experienced multiple ore-forming stages, and boiling in the main stage (Fig. 15A). The boiling might be closely related to the frequent tectonic activities in this area, and the

Table 8
Results of microthermometric, salinity, density, and trapping pressure in the Zhaishang gold deposit.

Stages of mineralization	Homogenization temperature (°C)	Ice point (°C)	Salinity (wt.%)	Density (g/cm^3)	Pressure (MPa)	Host mineral
Stage I	216–372 (292, n = 22)	−3.0 to −1.2 (−2.1, n = 22)	2.13–4.90 (3.55, n = 22)	0.80–1.03 (0.94, n = 22)	72.5–78.1 (76.4, n = 22)	Quartz
Stage II	131–293 (193, n = 47)	−10.4 to −1.6 (−2.7, n = 23)	0.70–8.14 (4.49, n = 23)	0.85–0.96 (0.93, n = 15)	38.9–52.9 (51.3, n = 15)	Quartz
Stage III	113–368 (186, n = 39)	−5.9 to −0.1 (−3.2, n = 24)	0.18–9.08 (5.26, n = 24)	0.71–0.99 (0.93, n = 24)	23.8–51.2 (49.9, n = 24)	Quartz
	92–278 (198, n = 30)	−6.1 to −0.1 (−2.6, n = 20)	0.18–9.34 (4.34, n = 20)	0.79–0.97 (0.88, n = 20)	25.3–54.5 (52.5, n = 20)	Calcite
Stage IV	106–288 (156, n = 99)	−25.6 to −0.4 (−7.3, n = 72)	0.70–23.11 (10.73, n = 73)	0.84–1.03 (0.96, n = 73)	31.2–53.5 (42.9, n = 73)	Quartz
	136–228 (159, n = 28)	−14.2 to −2.3 (−4.7, n = 19)	5.56–17.96 (7.59, n = 18)	0.89–0.98 (0.95, n = 18)	42.8–44.5 (43.5, n = 18)	Calcite
	140–194 (162, n = 16)	−23.2 to −3.1 (−16.4, n = 6)	5.11–22.52 (18.89, n = 6)	0.94–1.00 (0.97, n = 6)	43.4–45.5 (45.3, n = 6)	Ankerite
Stage V	144–197 (156, n = 27)	−7.1 to −1.4 (−4.5, n = 11)	2.41–10.61 (7.17, n = 11)	0.92–0.97 (0.96, n = 11)	39.3–43.1 (42.5, n = 11)	Calcite
	168–197 (183, n = 6)	–	–	–	–	Quartz
	105–194 (158, n = 19)	−3.4 to −0.8 (−2.3, n = 14)	1.40–5.56 (3.87, n = 14)	0.90–0.96 (0.93, n = 14)	36.9–42.6 (41.6, n = 14)	Barite

Note: "–" was not detected.
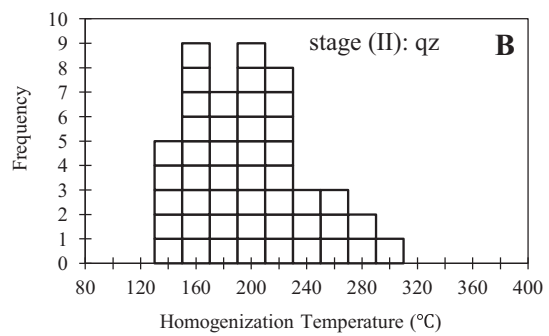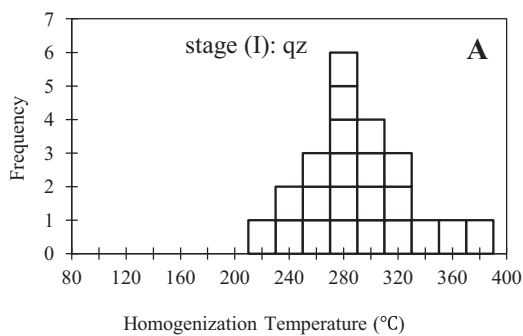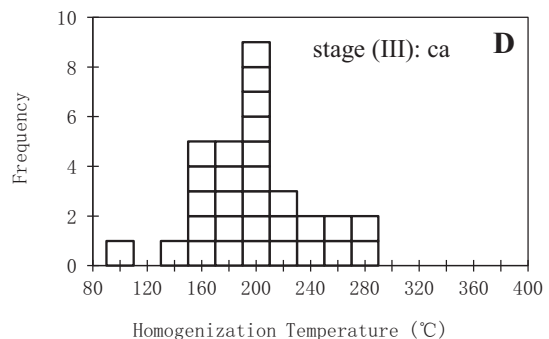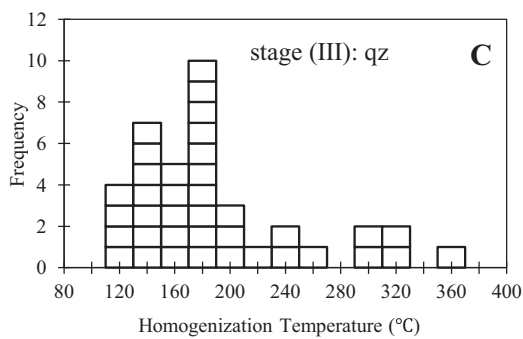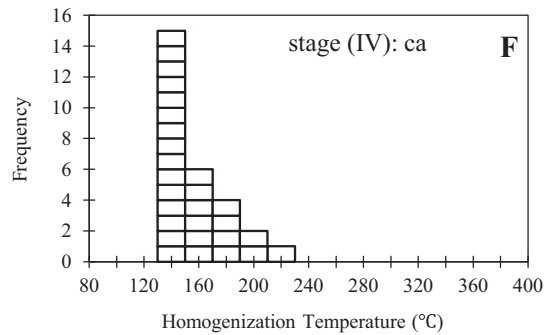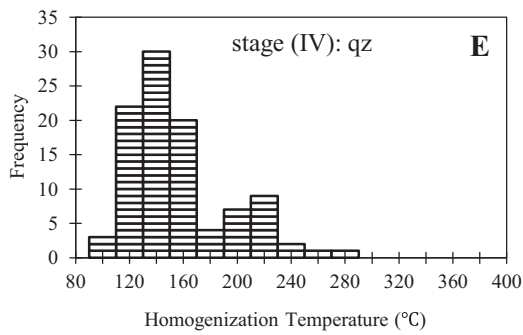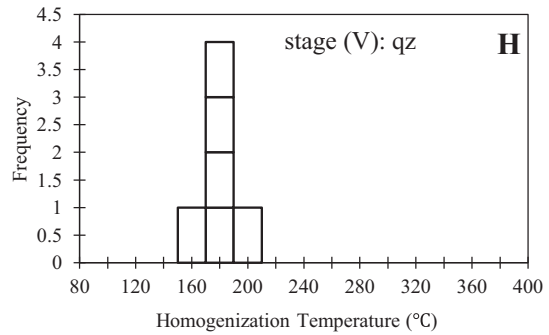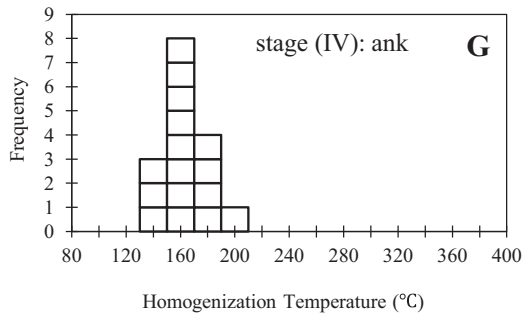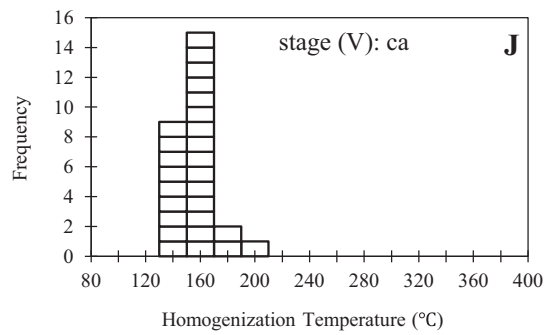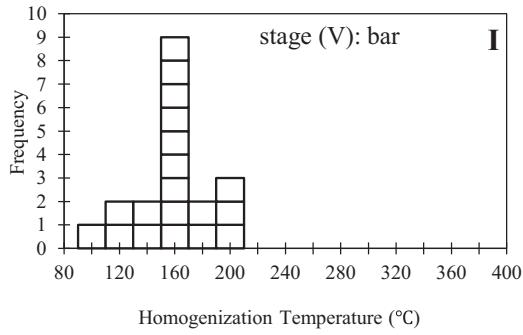
Table 9
Composition of vapor phase and liquid phase in fluid inclusions from the Zhaizhang gold deposit.

Seq. No.	Sample No.	Mineral	Li$^+$ (μg/g)	Na$^+$ (μg/g)	K$^+$ (μg/g)	Mg^{2+} (μg/g)	Ca^{2+} (μg/g)	F$^-$ (μg/g)	Cl$^-$ (μg/g)	NO$_3^-$ (μg/g)	SO$_4^{2-}$ (μg/g)
1	06zs-68	Quartz	–	4.316	2.79	–	4.158	0.040	3.691	0.419	9.026
2	06zs-81-2	Quartz	–	16.725	–	–	8.960	0.037	23.422	0.736	1.877
3	06zs-31	Quartz	–	2.867	–	–	5.985	0.137	7.515	0.548	1.199
4	06zs-24	Quartz	–	–	–	–	3.214	0.059	3.348	0.474	2.266
5	06zs-15	Quartz	–	3.168	3.278	–	2.683	0.119	2.253	0.476	4.111
6	06zs-39	Quartz	–	2.787	–	–	2.990	0.038	3.177	0.278	7.527

Seq. No.	Sample No.	Mineral	Sample temperature °C	CH$_4$ (μg/g)	C$_2$H$_2$ + C$_2$H$_4$ (μg/g)	C$_2$H$_6$ (μg/g)	CO$_2$ (μg/g)	H$_2$O (L) (μg/g)	O$_2$ (μg/g)	N$_2$ (μg/g)	CO (μg/g)
1	06zs-68	Quartz	100–500	6.344	0.135	0.054	140.880	498.016	10.988	114.001	–
2	06zs-81-2	Quartz	100–500	0.385	0.168	0.017	124.280	775.100	12.194	89.757	–
3	06zs-31	Quartz	100–500	2.079	0.121	0.024	106.958	367.279	5.527	79.024	–
4	06zs-24	Quartz	100–500	5.452	0.312	0.051	152.630	330.223	17.197	143.261	11.688
5	06zs-15	Quartz	100–500	0.518	0.419	0.111	99.667	177.748	–	57.625	–
6	06zs-39	Quartz	100–500	0.838	0.218	0.034	117.864	233.894	7.228	87.253	–

Note: Sequence Nos. 1–6 samples were analyzed at the Mineral Resources Research Institute, Chinese Academy of Geological Sciences.
Test equipment: Shimadzu GC2010 gas chromatograph, Shimadzu HIC-SP Super ion chromatograph, Australia SGE company burst hot stove.
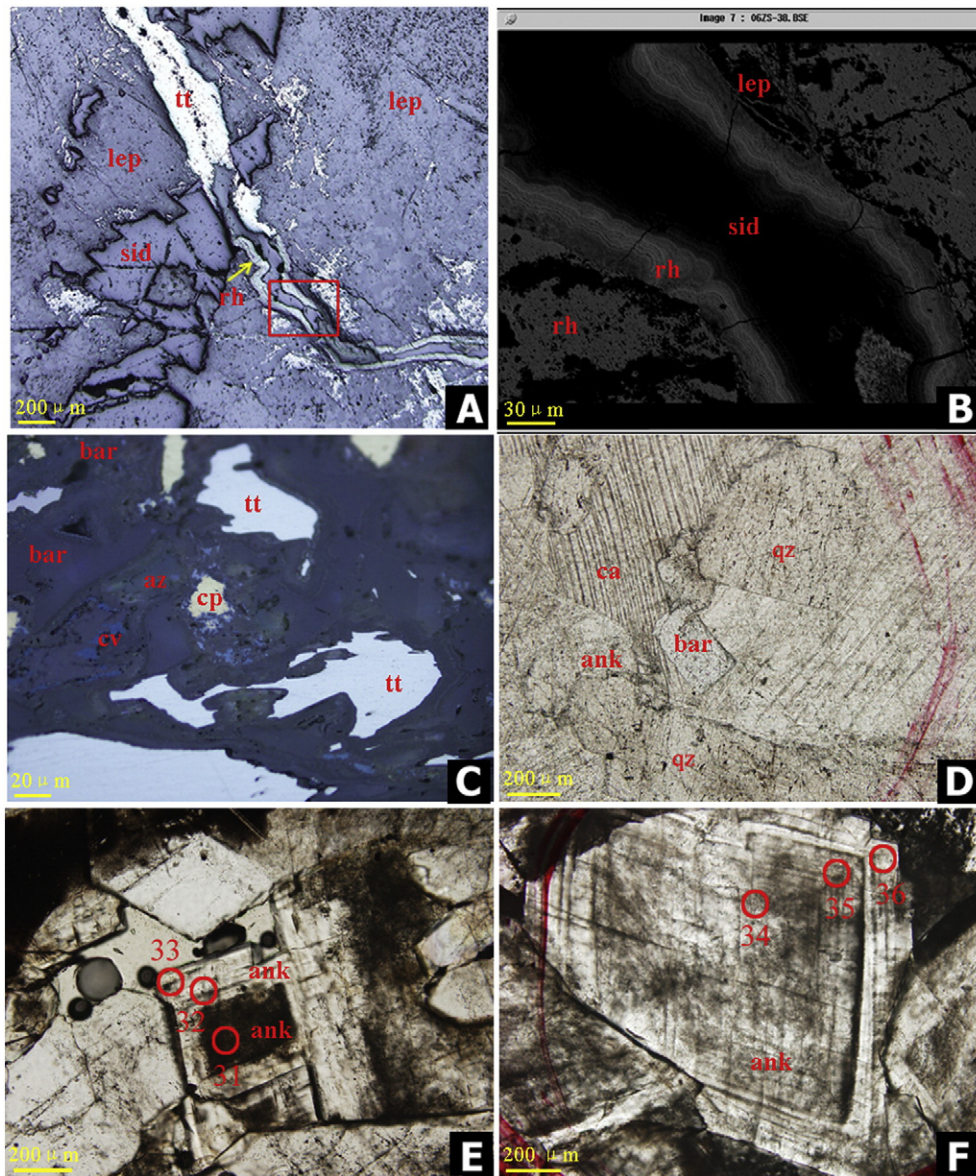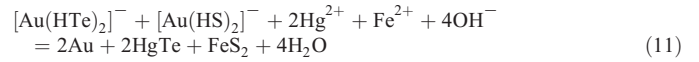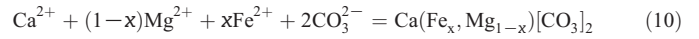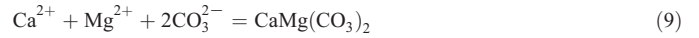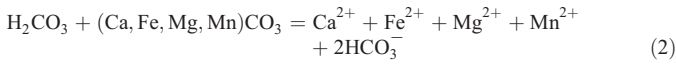Standard substance source: National Standard Substance Center, "–" represents not detected.

rapid pressure decrease was the main factor that caused the boiling. The change of pressure in hydrothermal conditions at the trap site promoted a large scale of metal sulfides and gold to precipitate, so it was an important turning point in mineralization. Decarbonatization could be the specific precipitation mechanism (Peters, 2004; Su et al., 2008).

It is well known that the chemical state of "invisible" gold is very difficult to study in sediment-hosted disseminated gold deposits because of the finely dispersed state of gold and sulfide grains (Liang et al., 2014). Previous studies employing electron microprobe analysis (EMPA) (Wells and Mullens, 1973), Mössbaur effect (Friedl et al., 1995), X-ray photoelectron spectroscopy (XPS) (Liang et al., 2012; Maddox et al., 1998; Mikhlin et al., 2011), X-ray absorption spectroscopy (XAS) (Mikhlin et al., 2011), X-ray absorption near-edge structure (XANES) (Simon et al., 1999a), and extended X-ray absorption fine structure spectroscopy (EXAFS) (Simon et al., 1999b), scanning tunneling microscopy (STM) (Mikhlin et al., 2011) and tunneling spectroscopy (STS) (Mikhlin et al., 2011), suggested that Au is most likely present as either Au^0 or Au^{1+}. Some significant advances have been made during recent years, for example, a solubility relationship between As and Au in arsenian pyrite was established, which predicted two states of both solid solution (Au^{1+}) and nanoparticle (Au^0) coexisted in sulfides (Reich et al., 2005). A number of mineralogical studies about Au in sulfides on submicron-sized scale in recent years have discovered that As is closely associated with Au (Cline, 2001; Cook and Chryssoulis, 1990; Fleet et al., 1993; Mumin et al., 1994; Reich et al., 2005; Savage et al., 2000), suggesting that significant substitution of As for S in pyrite lattice facilitates Au entering the pyrite structure (Ciobanu et al., 2011; Kovalev et al., 2008; Morishita et al., 2008; Palenik et al., 2004; Reich et al., 2005, 2010). It has been proposed that considerable stacking faults and lattice dislocations in pyrite due to such substitution create space for the large ionic size of Au^{+1} (0.137 nm) (Deditius et al., 2008; Palenik et al., 2004; Simon et al., 1999a). Reich et al. (2005) further suggested that the presence of native Au particles in pyrites depends on the saturation state of the hydrothermal solution. Au^0 is saturated or supersaturated in ore-forming fluids in epithermal systems, but is undersaturated in those associated with Carlin-type or sediment-hosted gold deposits. This explains the dominance of invisible gold in Carlin-type gold deposits, however, the mechanism of invisible native gold formation in these deposits remain unclear. Nanoparticles of native gold were identified under high-resolution TEM (Palenik et al., 2004; Reich et al., 2005, 2010), and the contents and distribution of Au in individual pyrite grains were determined by LA–ICP-MS imaging (Ciobanu et al., 2009;

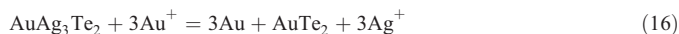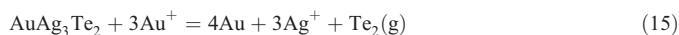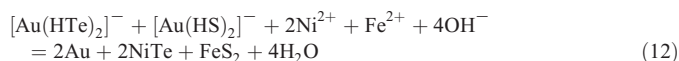Large et al., 2007, 2009; Su et al, 2009; Zacharias et al., 2004). These studies indicated that in situ microanalytical techniques such as EMPA, HRTEM and LA–ICP-MS are powerful in constraining the contents, distribution and chemical states of gold in sulfides (Liang et al., 2014; Mikhlin et al., 2011). Therefore, in Carlin-like gold deposits, invisible gold and rare ultra fine gold (nanometer size) are two important existing forms of gold (Arehart, 1996; Hofstra et al., 2000). The distribution of gold and the existence of native gold particles in the Zhaishang gold deposit reflect the different enrichment patterns of gold in different mineralization stages: in the early stages of mineralization, because the ore-forming fluid had high fS_2 and low fO_2 (Ma et al., 2008), these were not only beneficial to forming a large number of sulfide minerals but also helpful for gold to enter into arsenian pyrite in the form of Au$^+$ and form a solid solution of invisible gold. With the mineralization and the precipitation of sulfides, the fS_2 kept decreasing and the fO_2 and fTe$_2$ relatively increased, resulting in the formation of telluride and oxysalt minerals and less sulfide minerals (Ahmad et al., 1987; Afifi et al., 1988a,b; Simon and Essene, 1996; Simon et al., 1997). Meanwhile, the solid solution gold, which co-precipitated with As in the early ore stages, may have exsolved (Zhang et al., 1999) and may have become fine native gold particles that were encapsulated in arsenian pyrite that formed in the early generation. Some relatively coarse native gold particles were concentrated on the surface of or around late arsenian pyrite. This phenomenon is explained as the supersaturation of gold in hydrothermal fluids (Su et al., 2008). Experimental results show that in neutral to weak acidic, reduced hydrothermal solutions, Au(HS)$_2^-$ is the main migration form of Au (Seward, 1973). When f Te$_2$/f S$_2$ in hydrothermal fluid reaches 10^{-4}–10^{-5}, Au migrates mainly in the form of tellurium compounds ([Au(HTe)$_2$]$^-$) (Mikulski, 2005; Plotinskaya et al., 2006). The study of fluid inclusion in the Zhaishang gold deposit (Ma et al., 2008) shows that there was a certain amount of CO$_2$ and very little Fe in ore-forming fluid, indicating that the ore-forming fluid is weakly acidic and lacking of Fe. Therefore, Fe in the sulfides (arsenian pyrite) of the Zhaishang gold deposit probably came from the stratum itself, especially from the dissolution of Ferric carbonate in the stratum. The massive sulfidation of the dissolved Fe could cause the supersaturation of gold which caused the aggregation of native gold. The chemical equations of the formation process are as follows:

$$CO_2 + H_2O = H_2CO_3 \tag{1}$$

Fig. 16. Histogram showing homogenization temperature of fluid inclusions in the Zhaishang gold deposit. A. Mineralization stage I. B. Mineralization stage II. C, D. Mineralization stage III. E, F, G. Mineralization stage IV. H, I, J. Mineralization stage V. Abbreviations: qz = quartz; ca = calcite; ank = ankerite; bar = barite.

$$H_2CO_3 + (Ca, Fe, Mg, Mn)CO_3 = Ca^{2+} + Fe^{2+} + Mg^{2+} + Mn^{2+} \\ + 2HCO_3^- \tag{2}$$

$$Au(HS)_2^- + 0.5H_2 = Au^0 + H_2S + HS^- \tag{3}$$

$$2H_2S + Fe^{2+} = FeS_2 + 2H^+ + H_2 \tag{4}$$

$$2HS^- + Fe^{2+} = FeS_2 + 2H^+ \tag{5}$$

$$Ca^{2+} + CO_3^{2-} = CaCO_3 \tag{6}$$

$$Fe^{2+} + CO_3^{2-} = FeCO_3 \tag{7}$$

$$Mn^{2+} + CO_3^{2-} = MnCO_3 \tag{8}$$

$$Ca^{2+} + Mg^{2+} + 2CO_3^{2-} = CaMg(CO_3)_2 \tag{9}$$

$$Ca^{2+} + (1-x)Mg^{2+} + xFe^{2+} + 2CO_3^{2-} = Ca(Fe_x, Mg_{1-x})[CO_3]_2 \tag{10}$$

$$[Au(HTe)_2]^- + [Au(HS)_2]^- + 2Hg^{2+} + Fe^{2+} + 4OH^- \\ = 2Au + 2HgTe + FeS_2 + 4H_2O \tag{11}$$

Fig. 17. Carbonate and sulfate minerals of the gold ores. A. Siderite, rhodochrosite and tetrahedrite vein in oxidation ore, photomicrograph is in reflected light, sample 07ZS-38. B. Back-scattered electron image of the area in the red outlined box on the photograph A, sample 07ZS-38. C. Relationship barite with tetrahedrite, chalcopyrite, covellite and azurite, photomicrograph is in reflected light, sample 06ZS-51. D. Coexistence of barite with ankerite and quartz in calcite vein, thin section, sample 07ZS-61. E. Dolomite–ankerite zone, thin section, sample 07ZS-49. F. Dolomite–ankerite zone, thin section, sample 06ZS-48. Abbreviations: cp = chalcopyrite; tt = tetrahedrite; cv = covellite; az = azurite; lep = lepidokrocite; sid = siderite; rh = rhodochrosite; ank = ankerite; ca = calcite; qz = quartz; bar = barite. The figures on photographs E and F are the locations of the electron microprobe analysis.

$$[Au(HTe)_2]^- + [Au(HS)_2]^- + 2Ni^{2+} + Fe^{2+} + 4OH^-$$
$$= 2Au + 2NiTe + FeS_2 + 4H_2O \tag{12}$$

$$AuTe_2 + 2H_2O = Au + 2HTe^- + 2H^+ + O_2(g) \tag{13}$$

$$AuTe_2 = Au + Te_2(g) \tag{14}$$

$$AuAg_3Te_2 + 3Au^+ = 4Au + 3Ag^+ + Te_2(g) \tag{15}$$

$$AuAg_3Te_2 + 3Au^+ = 3Au + AuTe_2 + 3Ag^+ \tag{16}$$

$$AuAg_3Te_2 + 3Au^+ + 3Te_2(g) = 4AuTe_2 + 3Ag^+ \tag{17}$$

Based on the characteristics of mineral assemblages in the orebodies of the Zhaishang gold deposit, especially the close paragenesis among native gold, ankerite and arsenian pyrite, the formation process of microscopic native gold in the ores could be explained as: (1) the weak acid character of an ore-bearing hydrothermal fluid caused the dissolution of the Fe and Mn-bearing carbonate, releasing Fe, Ca, Mg, and Mn into the ore-bearing hydrothermal fluid system (chemical reactions 1–2); (2) the massive sulfidation of the dissolved Fe and the calcite, siderite, rhodochrosite, dolomite and ankerite veins (Fig. 17) which was formed by the combination of other dissolved Fe, Ca, Mg, Mn and CO_3^{2-}, caused the supersaturation and precipitation of Au which lead to the formation of native gold particles in an assemblage with arsenian pyrite and ankerite (Fig. 4B, C) (chemical reactions 3–10); (3) when the fS_2 decreased and fTe_2/fS_2 increased, gold migrated in the form of tellurium compounds ($[Au(HTe)_2]^-$). Because of the increase of the pH of the ore-forming fluid and the change in temperature, pressure and other factors, the soluble tellurium compounds ($[Au(HTe)_2]^-$) were destabilized, which caused the precipitation of gold and some tellurides (Figs. 4A, C; 6A, B, C) (chemical reactions 11–17).

Therefore, ferric carbonate minerals in the wall rock dissolving and releasing Fe, and massive sulfidation of dissolved Fe, are not only the most important factors of the existence of native gold, but also provided favorable conditions for precipitation and enrichment of gold in the Zhaishang gold deposit.

7. Conclusions

(1) The Zhaishang gold deposit has a rich mineral diversity. It has not only many sulfide, sulfsalt, oxide and oxysalt minerals, but also telluride, natural metals and alloys, etc. The diversity of mineral species in the ores and the occurrence of microscopic visible native gold are the outstanding features of this gold deposit.

(2) The study of the REE distribution pattern and isotopic compositions (carbon, lead, sulfur, oxygen and hydrogen) shows that ore-forming metals were mainly derived from the host sedimentary rocks and underlying rocks, and many partially from a deep source being associated with magmatic activity. Ore-forming hydrothermal fluid was mainly derived from heated cycling groundwater recharged by meteoric water. Mineralization and alteration proceeded in a low water/rock ratio system.

(3) Ferric carbonate minerals in the wall rock dissolved and released Fe, with massive sulfidation of dissolved Fe, leading to the precipitation of native gold in the Zhaishang gold deposit. The ore-forming hydrothermal fluid is low in temperature, salinity and density. After the full extraction of mineral material from sedimentary basin rocks, the charged original hydrothermal fluid evolved to become a rich-ore fluid, and deposited ore in a favorable position through boiling which was caused by pressure release.

References

Afifi, A.M., Kelly, W.C., Esscue, E.J., 1988a. Phase relations among tellurides, sulfides, and oxides: I. Thermochemical data and calculated equilibria. Econ. Geol. 83, 377–394.

Afifi, A.M., Kelly, W.C., Esscue, E.J., 1988b. Phase relations among tellurides, sulfides, and oxides: II. Thermochemical data and calculated equilibria. Econ. Geol. 83, 395–404.

Ahmad, M., Solomon, M., Walshe, J.L., 1987. Mineralogical and geochemical studies of the Emperor gold telluride deposit, Fiji. Econ. Geol. 82, 345–370.

Ames, L., Tilton, G.R., Zhou, G.Z., 1993. Timing of collision of the Sino-Korean and Yangtze cratons: U–Pb zircon dating of coesite-bearing eclogites. Geology 21, 339–342.

Arehart, G.B., 1996. Characteristics and origin of sediment-hosted gold deposits: a review. Ore Geol. Rev. 11, 383–403.

Boynton, W.V., 1984. Geochemistry of the rare-earth elements: meteorite studies. In: Henderson, P. (Ed.), Rare Earth Element Geochemistry. Elsevier, Amsterdam, pp. 63–114.

Cai, J.H., Zhang, Y.M., Fu, J.M., Chen, S.F., 1999. The genesis of the Yindonggou Ag-polymetallic deposit in the Northwest Hubei. Acta Geosci. Sin. 20, 316–320 (in Chinese with English abstract).

Cao, X.F., Lü, X.B., Yao, S.Z., Mei, W., Zou, X.Y., Chen, C., Liu, S.T., Zhang, P., Su, Y.Y., Zhang, B., 2011. LA–ICP-MS U–Pb zircon geochronology, geochemistry and kinetics of the Wenquan ore-bearing granites from West Qinling, China. Ore Geol. Rev. 43, 120–131.

Chen, Y.J., Zhang, J., Zhang, F.X., Franco, F., Li, C., 2004. Carlin and Carlin-like gold deposits in western Qinling Mountains and their metallogenic time, tectonic setting and model. Geol. Rev. 50, 134–152 (in Chinese with English abstract).

Chen, Z., Lu, S., Li, H., Li, H., Xiang, Z., Zhou, H., Song, B., 2006. Constraining the role of the Qinling Orogen in the assembly and break-up of Rodinia: tectonic implications for neoproterozoic granite occurrences. J. Asian Earth Sci. 28, 99–115.

Chen, Y.J., Pirajno, F., Qi, J.P., 2008. The Shanggong gold deposit, Eastern Qinling Orogen, China: isotope geochemistry and implications for ore genesis. J. Asian Earth Sci. 33, 252–266.

Ciobanu, C.L., Cook, N.J., Pring, A., Brugger, J., Danyushevsky, L.V., Shimizu, M., 2009. 'Invisible gold' in bismuth chalcogenides. Geochim. Cosmochim. Acta 73, 1970–1999.

Ciobanu, C.L., Cook, N.J., Utsunomiy, S., Pring, A., Green, L., 2011. Focused ion beam-transmission electron microscopy applications in ore mineralogy: bridging micro-and nanoscale observations. Ore Geol. Rev. 42, 6–31.

Claypool, G.E., Holser, W.T., Kaplan, I.R., Sakai, H., Zak, I., 1980. The age curves of sulfur and oxygen isotopes in marine sulfate and their mutual interpretation. Chem. Geol. 28, 199–260.

Clayton, R.N., 1986. High temperature isotope effects in the early solar system. In: Valley, J.W., Taylor Jr., O'Neil, J.R. (Eds.), Stable Isotopes in High Temperature Geological ProcessesRev. Mineral. 16, 129–139.

Clayton, R.N., Mayeda, T.K., 1963. The use of bromine pentafluoride in the extraction of oxygen from oxides and silicates for isotopic analysis. Geochim. Cosmochim. Acta 27, 43–52.

Cline, J.S., 2001. Timing of gold and arsenic sulfide mineral deposition at the Getchell Carlin-type gold deposit, north central Nevada. Econ. Geol. 96, 75–89.

Coleman, M.L., Sheppard, T.J., Durham, J.J., Rouse, J.E., Moore, G.R., 1982. Reduction of water with zinc for hydrogen isotope analysis. Anal. Chem. 54, 993–995.

Cook, N.J., Chryssoulis, S.L., 1990. Concentrations of invisible gold in the common sulfides. Can. Mineral. 28, 1–16.

Deditius, A.P., Utsunomiya, S., Renock, D., Ewing, R.C., Ramana, C.V., Becker, U., Kesler, S.E., 2008. A proposed new type of arsenian pyrite: composition, nanostructure and geological significance. Geochim. Cosmochim. Acta 72, 2919–2933.

Ding, T.P., Jiang, S.Y., Wan, D.F., Li, Y.H., Li, J.C., Song, H.B., Liu, Z.J., Yao, X.M., 1994. Silicon isotope geochemistry. Geology Press, Beijing, pp. 1–102 (in Chinese).

Doe, B.R., Zartman, R.E., 1979. Plumbotectonics. In: Barnes, H. (Ed.), Geochemistry of Hydrothermal Ore Deposits. John Wiley and Sons, New York, pp. 22–66.

Dong, Y., Zhang, G., Neubauer, F., Liu, X., Genser, J., Hauzenberger, C., 2011. Tectonic evolution of the Qinling Orogen, China: review and synthesis. J. Asian Earth Sci. 41, 213–237.

Fitoussi, C., Bourdon, B., Kleine, T., Oberli, F., Reynolds, B.C., 2009. Si isotope systematics of meteorites and terrestrial peridotites implications for Mg/Si fractionation in the solar nebula and for Si in the Earth's core. Earth Planet. Sci. Lett. 278, 286–296.

Fleet, M.E., Chryssoulis, S.L., Maclean, P.J., Davidson, R., Weisener, G.G., 1993. Arsenian pyrite from gold deposits — Au and As distribution investigated by SIMS and EMP, and color staining and surface oxidation by XPS and LIMS. Can. Mineral. 31, 1–17.

Friedl, J., Wagner, F.E., Wang, N., 1995. On the chemical state of combined gold in sulfidic ores — conclusions from Mossbauer source experiments. Neues Jb. Mineral. Abh. 169, 279–290.

Friedman, I., O'Neil, J.R., 1977. Compilation of stable isotope fractionation factors of geochemical interest, In: Fleischer, M. (Ed.), Data Geochemistry, 6th edition. United States Geological Survey Professional Paper. U.S. Geological Survey, Washington DC, (440-KK, 111 pp.).

Gao, S., Zhang, B., Wang, D., Ouyang, J., Xie, Q., 1996. Geochemical evidence for the Proterozoic tectonic evolution of the Qinling Orogenic Belt and its adjacent margins of the North China and Yangtze cratons. Precambrian Res. 80, 23–48.

Han, Y.G., Zhang, S.H., Pirajno, F., Zhang, Y.H., 2007. Evolution of the Mesozoic granites in the Xiong'ershan–Waifangshan region, western Henan Province, China, and its tectonic implications. Acta Geol. Sin. 81, 253–265.

Han, Y.G., Zhang, S.H., Pirajno, F., Zhou, X.W., Zhao, G.C., Qü, W.J., Liu, S.H., Zhang, J.M., Liang, H.B., 2013. U–Pb and Re–Os isotopic systematics and zircon Ce^{4+}/Ce^{3+} ratios in the Shiyaogou Mo deposit in eastern Qinling, central China: insights into the oxidation state of granitoids and Mo (Au) mineralization. Ore Geol. Rev. 55, 29–47.

He, H., Wei, L.M., Zhang, S.T., Gao, Y., Xu, Y., 2009. Helium, argon, hydrogen and oxygen isotopic characters of ore-forming fluid of the Baguamiao gold deposit in Shaanxi Province. Gold 30, 9–11 (in Chinese with English abstract).

Heberer, B., Anzenbacher, T., Neubauer, F., Genser, J., Dong, Y., Dunkl, I., 2014. Polyphase exhumation in the western Qinling Mountains, China: rapid Early Cretaceous cooling along a lithospheric-scale tear fault and pulsed Cenozoic uplift. Tectonophysics 617, 31–43.

Hofstra, A.H., Cline, J.S., 2000. Characteristics and models for Carlin-type gold deposits. In: Hagemann, S.G., Brown, P.E. (Eds.), Gold in 2000Rev. Econ. Geol. 13, 163–220.

Huang, C.H., Zhang, C.J., Liu, Z.H., 2010. Geological characteristics and genesis of the Jingdonggou gold deposit in Pingwu County, Sichuan Province. Geoscience 24, 18–25 (in Chinese with English abstract).

Ji, H.B., Li, C.Y., Wen, J.M., 1998. Source of ore-forming material and metallogenic age of the Zheboshan gold deposit, western Sichuan Province. China. Chin. Sci. Bull. 43, 684–690.

Keith, M.L., Weber, J.N., 1964. Carbon and oxygen isotopic composition of selected limestone and fossils. Geochim. Cosmochim. Acta 28, 1787–1816.

Khin, Z., Peters, S.G., Cook, N., Hou, Z.Q., 2007a. Preface—South China Mineral Deposits. In: Khin, Z., Peters, S.G., Cook, N., Hou, Z.Q. (Eds.), Special Issue on South China Mineral DepositsOre Geol. Rev. 19, 1–2.

Khin, Z., Peters, S.G., Cromie, P., Burrett, C., Hou, Z.Q., 2007b. Nature, diversity of types and metallogenic relations of South China. In: Khin, Z., Peters, S.G., Cook, N., Hou, Z.Q. (Eds.), Special Issue on South China Mineral Deposits, 2005Ore Geol. Rev. 31, 3–47.

Kovalev, K.R., Kalinin, Y.A., Naumov, E.A., Pirajno, F., Borisenko, A.S., 2008. A mineralogical study of the Suzdal sediment-hosted gold deposit, Eastern Kazakhstan: implications for ore genesis. Ore Geol. Rev. 35, 186–205.

Large, R.R., Maslennikon, V.V., Robert, F., Danyushevsky, L.V., Chang, Z.S., 2007. Multistage sedimentary and metamorphic origin of pyrite and gold in the giant Sukhoi Log deposit, Lena gold province, Russia. Econ. Geol. 102, 1233–1267.

Large, R.R., Danyushevsky, L.V., Hollit, C., Maslennikon, V.V., Meffre, S., Gilbert, S., Bull, S., Scott, R., Emsbo, P., Thomas, H., Singh, B., Foster, J., 2009. Gold and trace element zonation in pyrite using a laser imaging technique: implications for the timing of gold in orogenic and Carlin-style sediment-hosted deposits. Econ. Geol. 104, 635–668.

Li, S.G., Sun, W.D., Zhang, G.W., Chen, J.Y., Yang, Y.C., 1996. Chronology and geochemistry of metavolcanic rocks from Heigouxia Valley in the Mian–Lue tectonic zone, South Qinling: evidence for a Paleozoic oceanic basin and its close time. Sci. China Ser. D 39, 300–310.

Li, C., Chen, Y.J., He, S.D., 2001. East Qinling–Dabieshan lithosphere delaminating age, mechanism and direction petrological evidences and stipulation. Chin. J. Geochem. 20, 59–72.

Li, S.Z., Kusky, T.M., Wang, L., Zhang, G.W., Lai, S.C., Liu, X.C., Dong, S.W., Zhao, G.C., 2007. Collision leading to multiple-stage large-scale extrusion in the Qinling Orogen: insights from the Mianlue suture. Gondwana Res. 12, 121–143.

Li, N., Chen, Y.J., Santosh, M., Yao, J.M., Sun, Y.L., Li, J., 2011. The 1.85 Ga Mo mineralization in the Xiong'er Terrane, China: implications for metallogeny associated with assembly of the Columbia supercontinent. Precambrian Res. 186, 220–232.

Li, N., Ulrich, T., Chen, Y.J., Thomsen, T.B., Pease, V., Pirajno, F., 2012. Fluid evolution of the Yuchiling porphyry Mo deposit, East Qinling, China. Ore Geol. Rev. 48, 442–459.

Li, N., Deng, J., Yang, L.Q., Goldfarb, R.J., Zhang, C., Marsh, E., Lei, S.B., Koenig, A., Lowers, H., 2014. Paragenesis and geochemistry of ore minerals in the epizonal gold deposits of the Yangshan gold belt, West Qinling, China. Miner. Deposita 49, 427–449.

Liang, X.L., 2011. A number of large gold deposits were found at Gansu Province, China. Gold Sci. Technol. 19, 24 (in Chinese).

Liang, J.L., Sun, W.D., Li, Y.L., Zhu, S.Y., Li, H., Liu, Y.L., Zhai, W., 2012. An XPS study on the valence states of arsenic in arsenian pyrite: implications for Au deposition mechanism of the Yang-shan Carlin-type gold deposit, western Qinling belt. J. Asian Earth Sci. 62, 363–372.

Liang, J.L., Sun, W.D., Zhu, S.Y., Li, H., Liu, Y.L., Zhai, W., 2014. Mineralogical study of sediment-hosted gold deposits in the Yangshan ore field, Western Qinling Orogen, Central China. J. Asian Earth Sci. 85, 40–52.

Liu, X.H., 2006. Potential reserve prediction of the Jinlongshan gold deposit. Contrib. Geol. Miner. Resour. Res. 21, 118–120 (in Chinese with English abstract).

Liu, J.M., Liu, J.J., 1997. Basinal fluid genetic model of fine disseminated gold deposits in the Golden Triangle area between Yunnan, Guizhou and Guangxi. Acta Mineral. Sin. 17, 448–456 (in Chinese with English abstract).

Liu, S.F., Zhang, G.W., 2013. Mesozoic basin development and its indication of collisional orogeny in the Dabie orogeny. Chin. Sci. Bull. 58, 827–852.

Liu, Y.J., Cao, L.M., Li, Z.L., Wang, H.N., Chu, T.Q., Zhang, J.R., 1984. Element geochemistry. Geological Press, Beijing, pp. 244–257 (in Chinese).

Liu, J.J., Zheng, M.H., Liu, J.M., Su, W.C., 2000a. Geochemistry of the La'erma and Qiongmo Au–Se deposits in the western Qinling Mountains, China. Ore Geol. Rev. 17, 91–111.

Liu, J.J., Li, C.Y., Pan, J.Y., Hu, R.Z., Liu, X.F., Zhang, Q., 2000b. Isotopic geochemistry in the copper deposits from sandstone and shale in Lanping–Simao basin, western Yunnan. Mineral Deposits 19, 223–234 (in Chinese with English abstract).

Liu, J.J., He, M.Q., Li, Z.M., Liu, Y.P., Li, C.Y., 2004. The oxygen and carbon isotopic geochemistry and its significance in Baiyangping silver–copper polymetallic metallogenic concentration area, Lanping basin. Mineral Deposits 23, 1–10 (in Chinese with English abstract).

Liu, G.Z., Zheng, W.J., Liao, Y.F., 2006. Geology survey report of the Zhaishang gold deposit, Min County, Gansu Province. No. 5 Gold Geological Party of Chinese Armed Police Forcepp. 1–38 (in Chinese).

Liu, J.J., Zheng, M.H., Cook, N.J., Long, X.R., Deng, J., Zhai, Y.S., 2007. Geological and geochemical characteristics of the Sawaya'erdun gold deposit, southwestern Chinese Tianshan Mountains. Ore Geol. Rev. 32, 125–156.

Liu, J.J., Liu, G.Z., Liao, Y.F., Zheng, W.J., Yue, L.X., Hua, S.G., Mao, G.J., Wu, S.H., 2008a. Discovery and significance of scheelite orebodies in the Zhaishang gold deposit, southern Gansu. Geol. China 35, 1057–1064 (in Chinese with English abstract).

Liu, J.J., Mao, G.J., Ma, X.H., Li, L.X., Guo, Y.Q., Liu, G.Z., 2008b. Discovery of Cu–Ni–Zn–Sn–Fe alloy and S-bearing alloy in the Zhaishang gold deposit, southern Gansu Province and its geological significance. Sci. China Ser. D Earth Sci. 51, 769–777.

Liu, B.Z., Wang, J.P., Wang, K.X., Liu, J.J., Xie, H.Y., Cao, R.R., Hui, D.F., Cheng, J.J., 2011a. Characteristics and geological significance of fluid inclusions in the Shuangwang gold deposit, Shaanxi Province. Geoscience 25, 1088–1098 (in Chinese with English abstract).

Liu, X.H., Feng, M.S., Liu, J.J., Liu, M.W., Zhang, Y.W., 2011b. Research on the paragenetic relationship between tellurium and gold minerals in the Zhaishang gold deposit, western Qinling. Gold Sci. Technol. 19, 6–12 (in Chinese with English abstract).

Liu, C.H., Liu, J.J., Wang, J.P., Yang, L.B., Wu, J., Jia, L., 2013. Geochemical characteristics of rare earth elements and their implications for the Huachanggou gold deposit in Shaanxi Province, China. J. Rare Earths 31, 215–226.

Lu, Y.M., Li, H.G., Chen, Y.G., Zhang, G.L., Li, Z.H., 2006. Geological and geochemical features and origin of the Zhaishang gold deposit in the Min County, Gansu. Geol. Prospect. 42, 25–31 (in Chinese with English abstract).

Ma, J.W., Ao, H.H., Chen, S.D., 1997. Remote Sensing Geology of Cold Deposits in Qinling Mountains. Geological Press, Beijing, pp. 1–188 (in Chinese).

Ma, X.H., Liu, J., Li, L.X., Mao, G.J., Guo, Y.Q., 2008. The Zhaishang gold deposit in Gansu Province: characteristics, evolution of ore-forming fluids and their metallogenic implications. Acta Petrol. Sin. 24, 2069–2078 (in Chinese with English abstract).

Maddox, L.M., Bancroft, G.M., Scaini, M.J., Lorimer, J.W., 1998. Invisible gold: comparison of Au deposition on pyrite and arsenopyrite. Am. Mineral. 83, 1240–1245.

Mao, J.W., Qiu, Y.M., Goldfarb, J.R., Zhang, Z.C., Garwin, S., Ren, F.S., 2002. Geology, distribution, and classification of gold deposits in the western Qinling belt, central China. Miner. Deposita 37, 352–377.

Mao, J.W., Xie, G.Q., Bierlein, F., Qü, W.J., Du, A.D., Ye, H.S., Pirajno, F., Li, H.M., Guo, B.J., Li, Y.F., Yang, Z.Q., 2008. Tectonic implications from Re–Os dating of Mesozoic molybdenum deposits in the East Qinling–Dabie orogenic belt. Geochim. Cosmochim. Acta 72, 4607–4626.

Mao, J.W., Xie, G.Q., Pirajno, F., Ye, H.S., Wang, Y.B., Li, Y.F., Xiang, J.F., Zhao, H.J., 2010. Late Jurassic–Early Cretaceous granitoid magmatism in Eastern Qinling, central-eastern China: SHRIMP zircon U–Pb ages and tectonic implications. Aust. J. Earth Sci. 57, 51–78.

Mao, J.W., Pirajno, F., Cook, N., 2011a. Mesozoic metallogeny in East China and corresponding geodynamic settings — an introduction to the special issue. Ore Geol. Rev. 43, 1–7.

Mao, J.W., Pirajno, F., Xiang, J.F., Gao, J.J., Ye, H.S., Li, Y.F., Guo, B.J., 2011b. Mesozoic molybdenum deposits in the east Qinling–Dabie orogenic belt: characteristics and tectonic settings. Ore Geol. Rev. 43, 264–293.

McCrea, J.M., 1950. The isotopic chemistry of carbonates and a paleotemperature scale. J. Chem. Phys. 18, 849–857.

Mei, Z., Meng, Q., Cui, Z., Qu, H., 1999. Devonian depositional system and paleogeographic evolution of Qinling orogenic belt. J. Palaeogeogr. 1, 32–40.

Meng, Q.R., Zhang, G.W., 2000. Geologic framework and tectonic evolution of the Qinling Orogen, central China. Tectonophysics 323, 183–196.

Mikhlin, Y., Romanchenko, A., Likhatski, M., Karacharov, A., Erenburg, S., Trubina, S., 2011. Understanding the initial stages of precious metals precipitation: nanoscale metallic and sulfidic species of gold and silver on pyrite surfaces. Ore Geol. Rev. 42, 47–54.

Mikulski, S.Z., 2005. The telluride mineralization event(s) within the late-variscan gold deposits in the western Sudetes (NE part of the Bohemian massif, SW Poland): In:

Mao, J.W., Bierlein, F.P. (Eds.), Mineral Deposit Research: Meeting the Global Challenge, 2. Springer, pp. 1415–1418.

Morishita, Y., Shimada, N., Shimada, K., 2008. Invisible gold and arsenic in pyrite from the high-grade Hishikari gold deposit, Japan. Appl. Surf. Sci. 255, 1451–1454.

Mumin, A.H., Fleet, M.E., Chryssoulis, S.L., 1994. Gold mineralization in As-rich mesothermal gold ores of the Bogosu–Prestea mining district of the Ashanti gold belt, Ghana: remobilization of "invisible" gold. Miner. Deposita 29, 445–460.

O'Neil, J.R., Silberman, M.L., 1974. Stable isotope relations in epithermal Au–Ag deposits. Econ. Geol. 69, 902–909.

O'Neil, J.R., Clayton, R.N., Mayeda, T.K., 1969. Oxygen isotope fractionation in divalent metal carbonates. J. Chem. Phys. 51, 5547–5558.

Ohmoto, H., 1972. Systematics of sulfur and carbon isotopes in hydrothermal ore deposits. Econ. Geol. 67, 551–578.

Ohmoto, H., Rye, R.O., 1979. Isotope of sulfur and carbon, In: Barnes, H.L. (Ed.), Geochemistry of Hydrothermal Ore Deposits, 2nd ed. John Wiley and Sons, New York, pp. 509–567.

Palenik, C.S., Utsunomiya, S., Reich, M., Kesler, S.E., Wang, L.M., Ewing, R.C., 2004. "Invisible" gold revealed: direct imaging of gold nanoparticles in a Carlin-type deposit. Am. Mineral. 89, 1359–1366.

Peters, S.G., 2004. Syn-deformational features of Carlin-type Au deposits. J. Struct. Geol. 26, 1007–1023.

Peters, S.G., Huang, J.Z., Jin, C.Q., Li, Z.P., 2002a. Chapter 1. Introduction to and classification of sedimentary-rock-hosted deposits in P. R. China. In: Peters, S.G. (Ed.), Geology, Geochemistry, and Geophysics of Sedimentary Rock-hosted Au Deposits in P. R. China. U. S. Geological Survey Open-File Report 02-131, pp. 1–60.

Peters, S.G., Huang, J.Z., Jin, C.Q., 2002b. Chapter 4. Geology and geochemistry of sedimentary rock-hosted Au deposits in the Qin Ling fold belt (Chuan–Shan–Gan) area, Shannxi, Sichuan, and Gansu Provinces, P. R. China. In: Peters, S.G. (Ed.), Geology, Geochemistry, and Geophysics of Sedimentary Rock-hosted Au Deposits in P. R. China. U. S. Geological Survey Open-File Report 02-131, pp. 167–254.

Peters, T.J., Ayers, J.C., Gao, S., Liu, X.M., 2013. The origin and response of zircon in eclogite to metamorphism during the multi-stage evolution of the Huwan Shear Zone, China: insights from Lu–Hf and U–Pb isotopic and trace element geochemistry. Gondwana Res. 23, 726–747.

Plotinskaya, O.Yu., Kovalenker, V.A., Seltmann, R., Stanley, C.J., 2006. Te and Se mineralogy of the high-sulfidation Kochbulak and Kairagach epithermal gold telluride deposits (Kurama Ridge, Middle Tien Shan, Uzbekistan). Mineral. Petrol. 87, 187–207.

Qin, Z.Y., Lei, S.H., 1996. New information on the ages of the Wudang Group—with a discussion. Reg. Geol. China 2, 176–185 (in Chinese with English abstract).

Qin, J.F., Lai, S.C., Rodney, G., Diwu, C.R., Ju, Y.J., Li, Y.F., 2009. Geochemical evidence for origin of magma mixing for the Triassic monzonitic granite and its enclaves at Mishulingin the Qinling Orogen (central China). Lithos 112, 259–276.

Qiu, H.N., Wijbrans, J.R., 2006. Paleozoic ages and excess ^{40}Ar in garnets from the Bixiling eclogite in Dabieshan, China: new insights from ^{40}Ar/^{39}Ar dating by stepwise crushing. Geochim. Cosmochim. Acta 70, 2354–2370.

Reich, M., Kesler, S.E., Utsunomiya, S., Palenik, C.S., Chryssoulis, S.L., Ewing, R.C., 2005. Solubility of gold in arsenian pyrite. Geochim. Cosmochim. Acta 69, 2781–2796.

Reich, M., Chryssoulis, S.L., Deditius, A., Palacios, C., Zuniga, A., Weldt, M., Alvear, M., 2010. "Invisible" silver and gold in supergene digenite ($Cu_{1.8}$S). Geochim. Cosmochim. Acta 74, 6157–6173.

Robin, M.B., Joaquin, R., Spencer, R.T., Richard, M.T., Joseph, L.W., 1999. Lead isotope compositions of late cretaceous and early tertiary igneous rocks and sulfide minerals in Arizona: implications for the sources of plutons and metals in porphyry copper deposits. Econ. Geol. 94, 211–244.

Savage, K.S., Tingle, T.N., O'Day, P.A., Waychunas, G.A., Bird, D.K., 2000. Arsenic speciation in pyrite and secondary weathering phases, mother lode gold district Tuolumne County, California. Appl. Geochem. 15, 1219–1244.

Seward, T.M., 1973. The complexes of gold and the transport of gold in hydrothermal ore solutions. Geochim. Cosmochim. Acta 37, 370–399.

Shao, S.C., Wang, D.B., 2001. ^{39}Ar–^{40}Ar dating of three typical gold deposits and its geological significance in the Southern Qinling region. Acta Geol. Sin. 75, 106–110 (in Chinese with English abstract).

Sheppard, S.M.F., 1986. Characterization and isotopic variations in natural waters. In: Valley, J.W., Taylor Jr., H.P., O'Neil, J.R. (Eds.), Stable Isotopes in High Temperature Geological ProcessesRev. Mineral. 16, 165–183.

Simon, G., Essene, E.J., 1996. Phase relation among selenides, sulfides, tellurides, and oxides: I. Thermodynamic data and calculated equilibria. Econ. Geol. 91, 1183–1208.

Simon, G., Kesler, S.E., Essene, E.J., 1997. Phase relation among selenides, sulfides, tellurides, and oxides: II. Application to seseninde-bearing ore deposits. Econ. Geol. 92, 468–484.

Simon, G., Huang, H., Penner-Hahn, J.E., Kesler, S.E., Kao, L.S., 1999a. Oxidation state of gold and arsenic in gold-bearing arsenian pyrite. Am. Mineral. 84, 1071–1079.

Simon, G., Kesler, S.E., Chryssoulis, S., 1999b. Geochemistry and textures of gold-bearing arsenian pyrite, Twin Creeks, Nevada: implications for deposition of gold in Carlin-type deposits. Econ. Geol. 94, 405–421.

Stein, H.J., Markey, R.J., Morgan, J.W., Du, A., Sun, Y., 1997. Highly precise and accurate Re–Os ages for molybdenite from the East Qinling molybdenum belt, Shaanxi Province, China. Econ. Geol. 92, 827–835.

Stein, H.J., Markey, R.J., Morgan, J.W., Hannah, J.L., Scherstén, A., 2001. The remarkable Re–Os chronometer in molybdenite: how and why it works. Terra Nova 13, 479–486.

Su, W.C., Xia, B., Zhang, H.T., Zhang, X.C., Hu, R.Z., 2008. Visible gold in arsenian pyrite at the Shuiyindong Carlin-type gold deposit, Guizhou, China: implications for the environment and processes of ore formation. Ore Geol. Rev. 33, 667–679.

Su, W.C., Heinrich, C.A., Pettke, T., Zhang, X.C., Hu, R.Z., Xia, B., 2009. Sediment-hosted gold deposits in Guizhou, China: products of wall-rock sulfidation by deep crustal fluids. Econ. Geol. 104, 73–93.

Su, B.X., Zhang, H.F., Sakyi, P.A., Ying, J.F., Tang, Y.J., Yang, Y.H., Qin, K.Z., Xiao, Y., Zhao, X.M., 2010. Compositionally stratified lithosphere and carbonatite metasomatism recorded in mantle xenoliths from the Western Qinling (Central China). Lithos 116, 111–128.

Sun, X.M., Norman, D.I., Sun, K., Chen, J.D., Chen, B.H., 2001. Light hydrocarbon composition of fluid inclusions and its constraints on ore genesis: a case study of the Songxi Ag (Sb) deposit, Eastern Guangong. Miner. Depos. 20, 15–22 (in Chinese with English abstract).

Sun, W.D., Li, S.G., Chen, Y.D., Li, Y.J., 2002. Timing of synorogenic granitoids in the South Qinling, central China: constraints on the evolution of the Qinling–Dabie orogenic belt. J. Geol. 110, 457–468.

Wang, A.J., Chen, Y., 2002. Geochemical characteristics of gold carrying minerals of Liba type gold deposit in Zhongcuan region of Li County, Gansu Province and its metallogenic signification. Miner. Resour. Geol. 16, 297–301 (in Chinese with English abstract).

Wang, P.A., Chen, Y.C., Pei, R.F., 1998. Regional metallogenic series and tectono-metallogenic cycles and evolution of the Qinling Orogen. Geological Press, Beijing, pp. 1–161 (in Chinese).

Wang, Y.T., Mao, J.W., Lu, X.X., Ye, A.W., 2002. ^{40}Ar–^{39}Ar dating and geological implication of auriferous altered rocks from the middle-deep section of Q875 gold-quartz vein in Xiaoqinling area, Henan, China. Chin. Sci. Bull. 47, 1750–1755.

Wang, K.Y., Yao, S.Z., Yang, Y.C., Dai, J.Z., 2004. Geological characteristics and origin of Manaoke fine-grained disseminated gold deposit in northwestern Sichuan Province. Mineral Deposits 23, 494–501 (in Chinese with English abstract).

Wang, X.X., Castro, A., Pedreira, R., Lu, X.X., Xiao, Q.H., 2011. Triassic granitoids of the Qinling Orogen, central China: genetic relationship of enclaves and rapakivi-textured rocks. Lithos 126, 369–387.

Welhan, J.A., 1988. Origin of methane in hydrothermal system. Chem. Geol. 71, 183–198.

Wells, J.D., Mullens, T.E., 1973. Gold-bearing arsenian pyrite determined by microprobe analysis, Cortez and Carlin Lode mines, Nevada. Econ. Geol. 68, 87–201.

Xiao, L., Zhao, Y.S., Pan, A.J., Han, X.J., Cui, L., Zou, Y.L., 2008. An analysis of gold ore-controlling regularity and resource potential of western Qinling region. Mineral Deposits 27 (S1), 46–54 (in Chinese with English abstract).

Xu, J.F., Castillo, P.R., Li, X.H., Yu, X.Y., Zhang, B.R., Han, Y.W., 2002a. MORB-type rocks from the Paleo-Tethyan Mian–Lueyang northern ophiolite in the Qinling Mountains, central China: implications for the source of the low ^{206}Pb/^{204}Pb and high^{143}Nd/^{144}Nd mantle component in the Indian Ocean. Earth Planet. Sci. Lett. 198, 323–337.

Xu, P.F., Liu, F.T., Ye, K., Wang, Q.C., Cong, B.L., Chen, H., 2002b. Flake tectonics in the Sulu Orogen in eastern China as revealed by seismic tomography. Geophys. Res. Lett. 29, 231–234.

Yan, J.P., Zhang, W.H., Zhang, Y.C., Jin, B.Y., Yuan, S.S., 2011. Metallogenic conditions and prospecting potential of the Jiawu gold belt, Qinghai Province. Gold Sci. Technol. 19, 35–40 (in Chinese with English abstract).

Yang, X.Y., Zheng, Z.Y., 2003. Gold anomaly analysis of the Zhaishang gold area, Gansu. Gold Geol. 9, 65–68 (in Chinese with English abstract).

Yang, H.S., Zhang, F.L., Yin, H.F., Lai, X.L., Yang, F.Q., 1996. Evolution and metallogenesis of the western Qinling orogenic belt. Acta Geol. Sichuan 16, 73–79.

Yang, T., Zhu, L.M., Wang, F., Gong, H.J., Lu, R.K., 2013a. Geochemistry, petrogenesis and tectonic implications of granitic plutons at the Liziyuan orogenic goldfield in the Western Qinling Orogen, central China. Geol. Mag. 150, 50–71.

Yang, Y., Chen, Y.J., Zhang, J., Zhang, C., 2013b. Ore geology, fluid inclusions and four-stage hydrothermal mineralization of the Shangfanggou giant Mo–Fe deposit in Eastern Qinling, central China. Ore Geol. Rev. 55, 146–161.

Yin, X.M., 2004. Potential analysis and prospective value for gold resources of western Qinling in Gansu province. Acta Geol. Gansu 13, 10–15 (in Chinese with English abstract).

Yu, J.Y., Li, J.Z., Li, Y., 2010. An approach to genesis of the Yangshan Au deposit in Gansu Province. Acta Geol. 30, 170–173 (in Chinese with English abstract).

Yue, L.X., Yang, G.X., Wang, Y.M., Liu, X.H., 2013. Comprehensive information prospecting model of the Zhaishang gold deposit in Gansu Province. Gold Sci. Technol. 21, 43–47.

Zacharias, J., Fryda, J., Paterova, B., Mihaljevic, M., 2004. Arsenopyrite and As-bearing pyrite from the Roudny deposit, Bohemian Massif. Mineral. Mag. 68, 31–46.

Zartman, R.E., Doe, B.R., 1981. Plumbotectonics — the model. Tectonophysics 75, 135–162.

Zeng, Q.T., McCuaig, T.C., Hart, C.J.R., Jourdan, F., Muhling, J., Bagas, L., 2012. Structural and geochronological studies on the Liba goldfield of the West Qinling Orogen, Central China. Miner. Deposita 47, 799–819.

Zhang, G.W., Zhang, Z.Q., Dong, Y.P., 1995. Nature of main tectono-lithostratigraphic units of the Qinling Orogen: implications for the tectonic evolution. Acta Geol. Sin. 11, 101–114 (in Chinese with English abstract).

Zhang, F.X., Ma, J.Q., Chen, Y.J., 1999. Geochemistry of gold and arsenium in Qinling Carlin-type gold deposits. Geochemistry 28, 453–463 (in Chinese with English abstract).

Zhang, G.W., Zhang, B.R., Yuan, X.C., Xiao, Q.H., 2000. Qinling Orogenic belt and continental dynamics. Science Press, Beijing (855 pp; (in Chinese with English abstract)).

Zhang, F.X., Ji, J.L., You, L.L., Fan, C.H., 2001. Comparative features of Carlin-para-Carlin type gold deposits in the South Qinling and gold deposits in other areas. Geol. Rev. 47, 492–499 (in Chinese with English abstract).

Zhang, X.J., Zhang, J., Jia, Y.S., Zhou, Q.W., 2002a. Geological and geochemical features of the Jinmuda gold deposit in northwestern Sichuan Province. Geol. Prospect. 38, 28–32 (in Chinese with English abstract).

Zhang, J., Chen, Y.J., Zhang, F.X., Li, C., 2002b. Geochemical study of ore fluid in Jinlongshan Carlin-type gold ore belt in southwestern Shaanxi Province. Mineral Deposits 21, 283–291 (in Chinese with English abstract).

Zhang, W.Y., Liu, F.J., Huang, C.Q., 2003. Metallogenic characteristics of the Baguamiao gold deposit of Fengxian County, Shaanxi Province and its exploration perspective in the

vicinity of the deposit. Miner. Resour. Geol. 17, 136–139 (in Chinese with English abstract).

Zhang, G.W., Dong, Y.P., Lai, S.C., Guo, A.L., Meng, Q.R., Liu, S.F., Chen, S.Y., Yao, A.P., Zhang, Z. Q., Pei, X.Z., Li, S.Z., 2004. Mianlue tectonic zone and Mianlue suture zone on southern margin of Qinling–Dabie orogenic belt. Sci. China Ser. D Earth Sci. 47, 300–316.

Zhang, Q., Yin, X.M., Yin, Y., Jin, W.J., Wang, Y.L., Zhao, Y.Q., 2009. Issues on metallogenesis and prospecting of gold and copper deposits related to adakite and Himalayan type granite in west Qinling. Acta Petrol. Sin. 25, 103–122 (in Chinese with English abstract).

Zhao, G.C., He, Y.H., Sun, M., 2009. The Xiong'er volcanic belt at the southern margin of the North China Craton: petrographic and geochemical evidence for its outboard position in the Paleo-Mesoproterozoic Columbia Supercontinent. Gondwana Res. 17, 145–152.

Zhao, X.F., Zhou, M.F., Li, J.W., Qi, L., 2013. Late Paleoproterozoic sedimentary rock-hosted stratiform copper deposits in South China: their possible link to the supercontinent cycle. Miner. Deposita 48, 129–136.

Zheng, Y.F., 1990. Carbon-oxygen isotopic covariations in hydrothermal calcite during degassing of CO_2: a quantitative evaluation and application to the Kushikino gold mining area in Japan. Miner. Deposita 25, 246–250.

Zheng, Y.F., 2001. The modeling of stable isotopic system and application for ore deposit geochemistry. Mineral Deposits 25, 246–250 (in Chinese with English abstract).

Zheng, Y.F., 2008. A perspective view on ultrahigh-pressure metamorphism and continental collision in the Dabie–Sulu orogenic belt. Chin. Sci. Bull. 53, 3081–3104.

Zheng, Y.F., Hoefs, J., 1993. Carbon and oxygen isotopic covariation in hydrothermal calcites. Miner. Deposita 28, 79–89.

Zheng, M.H., Zhou, Y.F., Liu, J.M., Gu, X.X., Liu, J.J., Schulz, O., Vavtar, F., 1994. Stratabound gold deposits of exhalation and turbidity type. Sichuan Science and Technology Press, Chengdu, pp. 146–170 (in Chinese with English abstract).

Zheng, J.P., Griffin, W.L., Sun, M., O'Reilly, S.Y., Zhang, H.F., Zhou, H.W., Xiao, L., Tang, H.Y., Zhang, Z.H., 2010. Tectonic affinity of the west Qinling terrane (central China): North China or Yangtze? Tectonics 29 (2), TC2009. http://dx.doi.org/10.1029/2008TC002428.

Zhu, R.X., Yang, Z.Y., Wu, H.N., Ma, X.H., Huang, B.C., Meng, Z.F., Fang, D.J., 1998. Palaeomagnetic constraints on the tectonic history of the major blocks of China during the Phanerozoic. Sci. China Ser. D Earth Sci. 41, 1–19.

Zhu, L.M., Zhang, G.W., Li, B., Guo, B., Kang, L., Lv, S.L., 2009. Geology, isotope geochemistry and ore genesis of the Ma'anqiao gold deposit, Shanxi Province. Acta Petrol. Sin. 25, 431–443 (in Chinese with English abstract).

Zhu, L.M., Zhang, G.W., Chen, Y.J., Ding, Z.J., Guo, B., Wang, F., Lee, B., 2011. Zircon U–Pb ages and geochemistry of the Wenquan Mo-bearing granitioids in West Qinling, China: constraints on the geodynamic setting for the newly discovered Wenquan Mo deposit. Ore Geol. Rev. 55, 46–52.

Zou, H.Y., Chen, S.L., Dai, T.G., 2000. Geology and ore forming fluid types of the Linxiang gold deposit. Xunyang, Shaanxi. Geotecton. Metallog. 24, 65–69 (in Chinese with English abstract).